ORNL/TM-2016/726

Design and Screening of Nanoprecipitates-Strengthened Advanced Ferritic Alloys

Lizhen Tan
Ying Yang
Tianyi Chen
Oak Ridge National Laboratory

Kumar Sridharan
Li He
University of Wisconsin-Madison

December 30, 2016

OAK RIDGE NATIONAL LABORATORY
MANAGED BY UT-BATTELLE FOR THE US DEPARTMENT OF ENERGY

ORNL/TM-2016/726
M2CA-15-TN-OR0402022

Nuclear Energy Enabling Technologies (NEET): Reactor Materials

DESIGN AND SCREENING OF NANOPRECIPITATES-STRENGTHENED ADVANCED FERRITIC ALLOYS

Lizhen Tan, Ying Yang, Tianyi Chen
Oak Ridge National Laboratory

Kumar Sridharan, Li He
University of Wisconsin-Madison

Date Published: December 30, 2016

Prepared by
OAK RIDGE NATIONAL LABORATORY
Oak Ridge, TN 37831-6283
managed by
UT-BATTELLE, LLC
for the
US DEPARTMENT OF ENERGY
under contract DE-AC05-00OR22725

CONTENTS

Page

LIST OF FIGURES

LIST OF TABLES

ACKNOWLEDGMENTS

This research was sponsored by the U.S. Department of Energy (DOE), Office of Nuclear Energy (NE), the Nuclear Energy Enabling Technologies (NEET) program, Reactor Materials FY 2015 Award. We gratefully acknowledge the support provided by Sue Lesica of DOE-NE and Stuart Maloy of Los Alamos National Laboratory.

The authors are grateful to David Harper and Tom Geer of Oak Ridge National Laboratory (ORNL) for alloy fabrication and sample preparation, and Kyle Blomstrand and Soham Shah of the University of Wisconsin-Madison for assistance in ion-irradiation sample preparation and some characterization. Philip Maziasz of ORNL is appreciated for technical review of this report.

EXECUTIVE SUMMARY

Advanced nuclear reactors as well as the life extension of light water reactors require advanced alloys capable of satisfactory operation up to neutron damage levels approaching 200 displacements per atom (dpa). Extensive studies, including fundamental theories, have demonstrated the superior resistance to radiation-induced swelling in ferritic steels, primarily inherited from their body-centered cubic (bcc) structure. This study aims at developing nanoprecipitates strengthened advanced ferritic alloys for advanced nuclear reactor applications. To be more specific, this study aims at enhancing the amorphization ability of some precipitates, such as Laves phase and other types of intermetallic phases, through smart alloying strategy, and thereby promote the crystalline→amorphous transformation of these precipitates under irradiation.

Reliability of computational thermodynamics primarily depends on thermodynamic database. Based on the recently developed database, nickel was identified to suppress the liquidus temperature of Fe_2Zr, and thus is added in the database to favor amorphorization tendency of the precipitates. A number of ferritic alloys and ferritic-martensitic steels were designed following the guidance of computational thermodynamics modeling. In addition to the four alloys (Z3N4, Z3N7, Z6N5, and Z6N9) used to justify and optimize the developing thermodynamic database, a total of two 12Cr ferritic alloys (Z2N13, Z1N33A) and two 9Cr ferritic-martensitic steels (53T1 and 63T1), together with one 15Cr ferritic alloy (2573) and one 9Cr ferritic-martensitic steel (TTZ2M) produced from a previous project, were fabricated and included in this work for mechanical property and radiation resistance screening tests.

The study of the four alloys Z3N4, Z3N7, Z6N5, and Z6N9 indicated that the phases in equilibrium with the matrix body-centered cubic phase are C15_Laves phase and $Fe_{23}Zr_6$ phase. The volume fraction of the intermetallic phases increased with the increasing Ni and Zr content. Instead of $(Fe,Cr)_2Zr$ C14_Laves phase, Ni stabilizes the C15_Laves structure in the Fe-Cr-Ni-Zr alloys by substituting Fe and Cr atoms with Ni atoms in the first sublattice. Addition of Ni also stabilized $Fe_{23}Zr_6$, which is metastable in the Fe-Cr-Zr ternary system. Additionally, Ni_7Zr_2 phase was observed in samples with high Ni/Zr ratio. Increasing the Zr and Ni content noticeably increased the hardness and strength of the alloys because of the increased fraction of intermetallic phases. The results suggest that this type of ferritic alloys should have Ni < ~4 wt.% and Zr < ~3 wt.% for balanced strength and ductility. The microstructural and composition results obtained from this study was incorportated into the the Fe-Cr-Ni-Zr database for further alloy design.

The two 12Cr ferritic alloys, i.e., Z2N13 and Z1N33A, were designed and fabricated to investigate effect of Laves phase and B2-NiAl phase on mechanical properties and radiation resistance. Compared to the 10–20 μm grain size of Z2N13, the grain size of Z1N33A is about one order of magnitude larger. The high density (10^{22} m^{-3}) of ultrafine (~11 nm) B2-NiAl precipitates in Z1N33A significantly increased the strength of the alloy at temperatures below 700°C. However, coarse Laves particle strings decorating boundaries resulted in brittle fracture of the alloy at room temperature. Alloy optimization will be proposed to eliminate the coarse Laves phase strings for satisfactory strength-ductility combination. Two 9Cr ferritic-martensitic steels, i.e., 53T1 (91TT) and 63T1 (91TTa), were designed to have different amounts of $M_{23}C_6$ and MX precipitates to understand the effects of the two types of precipitates on strength and radiation resistance. However, the two steels in the normalized and tempered condition did not exhibit significant differences in microstructures and tensile properties. Further microstructural characterization is in progress to elucidate this observation. Two TMTs were applied to the two steels, leading to significant or moderate increases in Vickers hardness. Microstructural characterization and tensile tests are in progress to understand the TMT effects.

One set of samples from eight of the ferritic and ferritic-martensitic alloys, i.e., Z3N4, Z3N7, Z2N13, Z1N33A, 2573, 53T1, and 63T1, was irradiated in two runs at 349 ± 12°C and 343 ± 21°C with 4 MeV

Fe^{2+} for up to 2.14×10^{17} ion/cm^2. The irradiation is expected to have a peak damage of ~218 dpa at 1.1 μm under surface according to the SRIM simulation. Post-irradiation characterization is in progress. Preliminary results indicated that all the irradiated samples had smooth and reflective surface. Similar radiation-induced hardening by ~20% at 1 μm indentation depth was observed on both Z2N13 and Z3N7. Irradiation resulted in a slight increase in precipitate size in 63T1 and TTZ2M. Detailed characterization is in progress.

1. INTRODUCTION

Advanced nuclear reactors as well as the life extension of light water reactors require advanced alloys capable of satisfactory operation up to neutron damage levels approaching 200 displacements per atom (dpa)[1]. Extensive studies, including fundamental theories, have demonstrated the superior resistance to radiation-induced swelling in ferritic steels, primarily inherited from their body-centered cubic (bcc) structure [2]. In our previous work [3], novel Fe-Cr-Zr ferritic alloys strengthened by Fe_2Zr_based Laves_phase precipitates show superior strength, ductility and creep resistance at high temperature, however, a consistent improvement on their irradiation resistance data have yet to be achieved. Amorphization of Fe_2Zr Laves phase has been frequently attained through mechanical alloying [4], sputtering deposition [5], and ion irradiation [6]. In a recent *in situ* ion irradiation study of a binary bcc(Fe)/Fe_2Zr nanocomposite, irradiation-induced amorphization of Fe_2Zr has been directly observed [7] under TEM. It was found that the density and size of the irradiation-induced defects such as dislocation loops is drastically low in the adjacent bcc matrix phase. In situ TEM revealed that the dislocation loops in Bcc(Fe) were confined by the crystal/amorphous interfaces and kept migrating to annihilate other defects. The amorphous Fe_2Zr nanolayer was also suggested as potential traps of the radiation-induced defects due to its excess free volume [7]. This study lends us new insights on the design of irradiation resistant Fe-Cr-Zr ferritic alloys.

Unlike the Fe_2Zr nanolayer in the Fe-Zr binary in literature [7], the Fe_2Zr nanoprecpitates formed in our Fe-Cr-Zr-based alloys still remain crystalline feature after irradiation. Preliminary TEM results clearly show the diffraction spots from crystalline Laves phase [8]. The lack of complete amorphization in our work can be attributed to several factors such as appreciable solubility of Cr in the Fe_2Zr phase, nonuniform sizes of Fe_2Zr particles, and unfavorable irradiation conditions. This incomplete amorphization can have a role in explaining the large scattering of the hardening data in the irradiated Fe-Cr-Zr-based (Z-) alloys [8]. While we could manipulate the irradiation conditions for complete amorphization, we propose to enhance the ability for amorphization of Fe_2Zr-based nanoprecipitates in the Fe-Cr-Zr alloys through smart alloying strategy, and thereby promote the crystalline→amorphous transformation of these precipitates under irradiation. With the enhanced ability for amorphization, the precipitates are expected to better tolerate different irradiation conditions and size difference, and reach a complete crystalline→amorphous transformation.

The challenge is to identify smart alloying strategy that can promote the amorphous-forming ability of the $(Fe,Cr)_2Zr$ Laves precipitates. The concept of the amorphous-forming ability is borrowed from the glass-forming ability (GFA) of a melt [9]. While it is often evaluated by the critical cooling rate required to bypass the formation of crystals, it is primarily determined by the alloy composition. The GFA of an alloy composition has been gauged using the criterion of $T_x/(T_g+T_l)$, where T_x, T_l and T_g are the onset crystallization (solidus), liquidus and glass transition temperature, respectively. The larger the value of $T_x/(T_g+T_l)$, the higher the GFA. For a particular alloy system, the T_g does not differ very much from one composition to the other. In contrast, the T_x and T_l can change significantly with composition as suggested by solidus and liquidus of a phase diagram. Clearly, by reducing T_l, i.e., suppressing the liquidus temperature, the GFA can be improved. Extensive studies have suggested that the high GFA is closely related to large atomic size mismatch, large negative enthalpy of formation and complex crystal structure [10]. These conditions are often manifested in systems with low lying liquid surface, such as eutectic reaction [11,12,13].

2. COMPUTATIONAL ALLOY DESIGN

The selection of alloying elements and the design of experimental alloy compositions were aided by computational thermodynamics. The essence of computational thermodynamics, i.e., the CALPHAD (CALculation of PHAse Diagram) approach [14], was to construct phase diagrams of multicomponent systems based on well assessed thermodynamic functions of Gibbs energy of phases. In the prior NEET project, a thermodynamic database containing major elements of Fe, Cr, Zr and minor elements of Mo, W, Si, Nb, C has been developed and validated by experimental data [8]. Ni were also included in this database but need to be further validated by experimental data. This database is used as a starting point for alloy design. The experimental data generated from these alloys will be used to validate the calculated results.

Computation screening on isopleth of Fe_2Zr –Fe_2X (X=Mo, W, and Nb) found all these alloying elements increase the liquidus temperature of Fe_2Zr. In contrast, Ni addition into the Fe-Cr system decreases the liquidus temperature of Fe_2Zr. The major difference between Ni and other alloying elements such as Mo, Nb and W is that the former mainly substitutes the Fe in the first sublattice while the others substitute the Zr in the second sublattice. Therefore, Ni is selected as an element that has potential to promote the amorphous forming ability of Fe_2Zr. Based on the preliminary Fe-Cr-Zr-Ni database, we calculated the liquidus surface of the Fe-Cr-Zr and Fe-Ni-Zr and compared them side by side in Figure 1 (a) and (b). The results suggest the Fe-Ni-Zr liquidus surface is more suppressed than that of Fe-Cr-Zr.

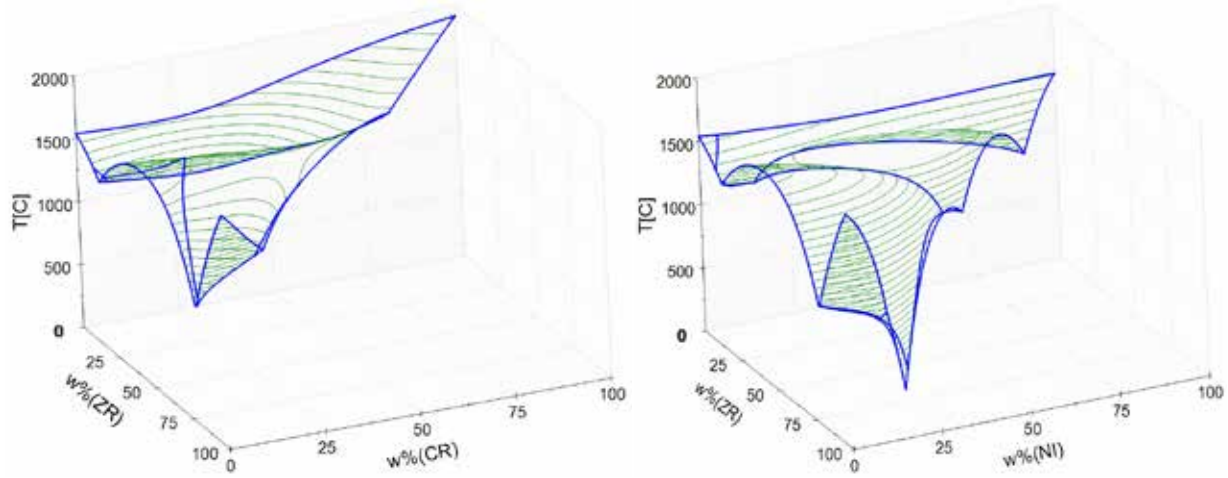

Figure 1. Calculated liquidus surfaces of (a) Fe-Cr-Zr and (b) Fe-Ni-Zr systems.

While it is difficult to visualize the liquidus surface in a quarternary system, we can plot different isopleth sections to see how Ni affects liquidus surface. Two isopleth section in the Fe-rich region were calculated and plotted in Figure 2 (a) and (b). One is the isopleth section with fixed Zr concentration at 33.3 at%. This isopleth essentially plots the phase diagram along M_2Zr (M=Fe,Cr, Ni) direction. We also need to fix another variable to obtain the 2D diagram. The Cr concentration is fixed at 12 wt%, as this amount of Cr is desired to reach desirable corrosion resistance. The results shows when increasing Ni concentration, the temperature of liquidus surface is decreasing. The second isopleth plots the phase diagram with fixed Cr and Ni concentration, in which a deep eutectic between Bcc(Fe) and Laves_C15 presents. Thermodynamic calculation suggests that adding Ni to the Fe-Cr-Zr alloy suppresses the liquidus surface in Fe-rich region, thus fufill our design goal. However, these results are exclusively from calculation. We need to validate the calculation results from experiments. Isothermal sections of Fe-Cr-Ni-Zr at 1000 and 700°C were calculated with fixed Cr concention at 12 wt%. The calculated results are shown in Figure 3 with the red line denoting phase boundaries at 700°C, and the black line for 1000 °C. Four alloy

compositions close to the phase boundary were selected for experimental study including isothermal annealing at 1000 and 700 °C. Annealing at two temperatures can help us to get an idea how stable the phase boundary vs temperature and whether to introduce an entropy term when modeling the Gibbs energy function.

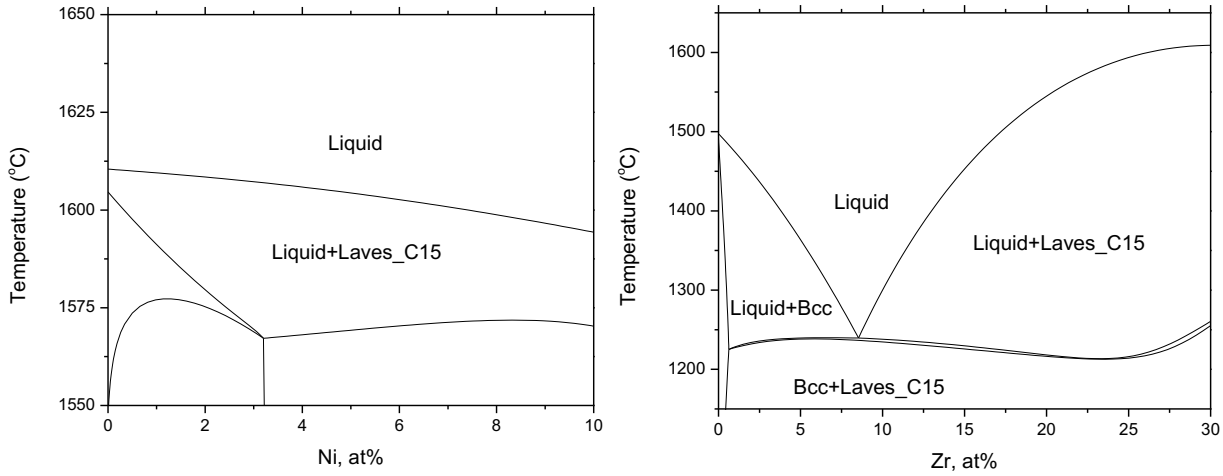

Figure 2. Isopleth sections in the Fe-Cr-Ni-Zr system with (a) fixed Cr at 13 at% and Zr at 33.3 at%; (b) fixed Cr at 13 at% and Ni at 5 at%.

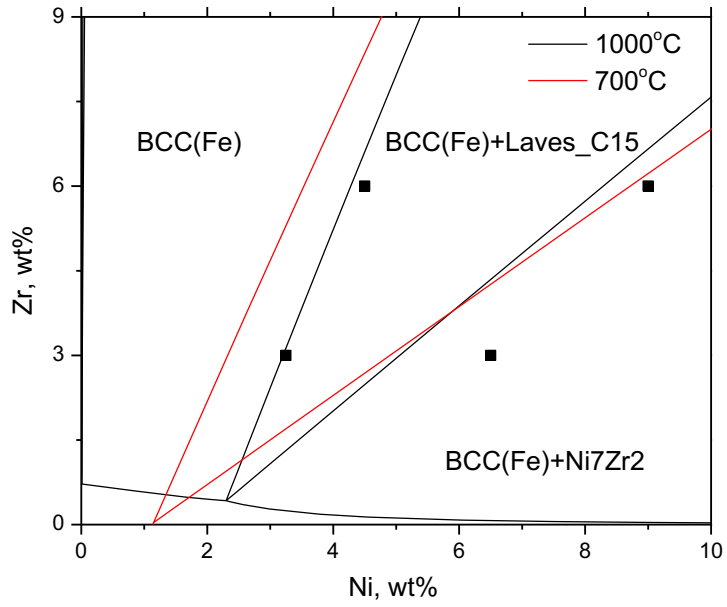

Figure 3. Fe-12Cr-Ni-Zr isothermal section at 1000 °C (black lines) and 700 °C (red lines) with the symbols denoting four alloys of Fe-12Cr-3Zr-3.25Ni, Fe-12Cr-3Zr-6.5Ni, Fe-12Cr-6Zr-4.5Ni, and Fe-12Cr-6Zr-9Ni to be experimentally studied.

By using the recently developed thermodynamic database [8,15], several ferritic and ferritic-martensitic steels were designed with the calculated temperature-dependent phase fractions of the alloys plotted in

Figure 4 and 5. Figure 4a shows two ferritic alloys Z3N4 (solid lines) and Z3N7 (dashed lines), having varied Ni content of 3.3 and 6.5 weight percentage (wt%), respectively, in Fe-12Cr-3Zr, which primarily resulted in the changes of Ni_7Zr_2 and Laves phase fractions. Figure 4b shows ferritic alloy Z2N13 (Fe-12Cr-1.5Zr-1Ni-3W), having significantly reduced austenite (γ) and the introduction of C15-type Laves phase, compared to the conventional C14-type Laves phase in Figure 4a. Figure 4c shows ferritic alloy Z1N33A (Fe-12Cr-1Zr-3Ni-3W-3Al), having eliminated austenite (γ) and the introduction of B2 phase, compared to Figure 4b. Figure 4d shows ferritic alloy 2573 (Fe-15Cr-1.5W-1Mo-0.35Nb-0.15Ti-0.04C), being composed of simple precipitates of MX and C14-type Laves phase.

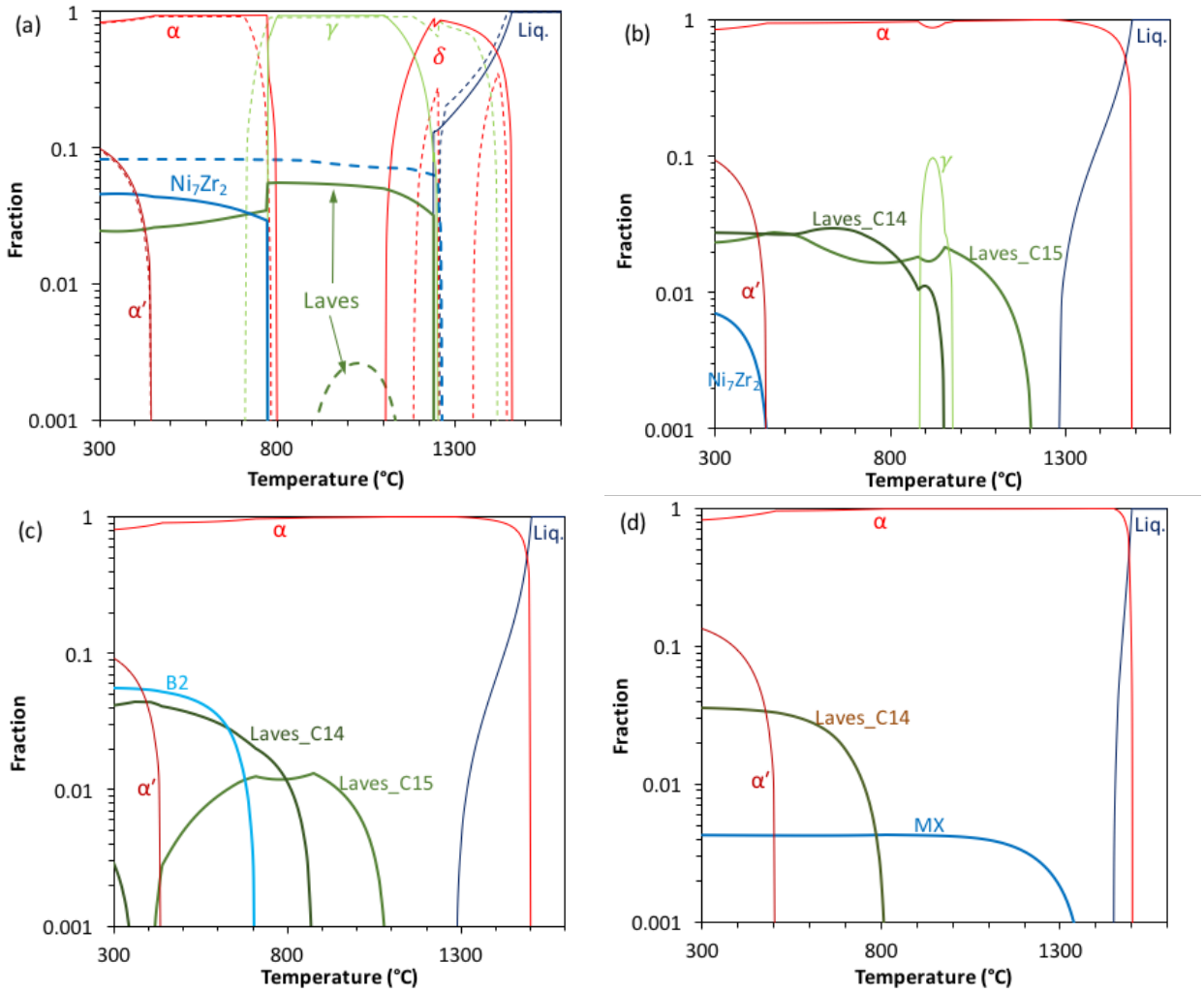

Figure 4. Calculated temperature-dependent phase fractions in five designed ferritic alloys of (a) Fe-12Cr-3Zr-3.3Ni (Z3N4, solid lines) and Fe-12Cr-3Zr-6.5Ni (Z3N7, dashed lines), (b) Fe-12Cr-1.5Zr-1Ni-3W (Z2N13), (c) Fe-12Cr-1Zr-3Ni-3W-3Al (Z1N33A), and (d) Fe-15Cr-1.5W-1Mo-0.35Nb-0.15Ti-0.04C (2573).

The three 9Cr ferritic-martensitic steels in Figure 5a were designed to eliminate the MX→Z phase transformation as shown in commercial 9Cr ferritic-martensitic steel T91 (Figure 5b). By adjusting the C/(Ti+Ta/Nb) ratio, the three designed ferritic-martensitic steels are expected to offer three comparison opportunities of:

- 53T1 (i.e., 91TT) vs T91 with comparable fractions of $M_{23}C_6$, MX, and Laves phases: discover the benefit of eliminating Z-phase;

- 53T1 (i.e., 91TT) vs 63T1 (i.e., 91TTa) with the same phase constituents: discover the benefit of MX over $M_{23}C_6$;
- 63T1 (i.e., 91TTa) vs TTZ2M with comparable fractions of the phases: discover different effects between Ta and Nb.

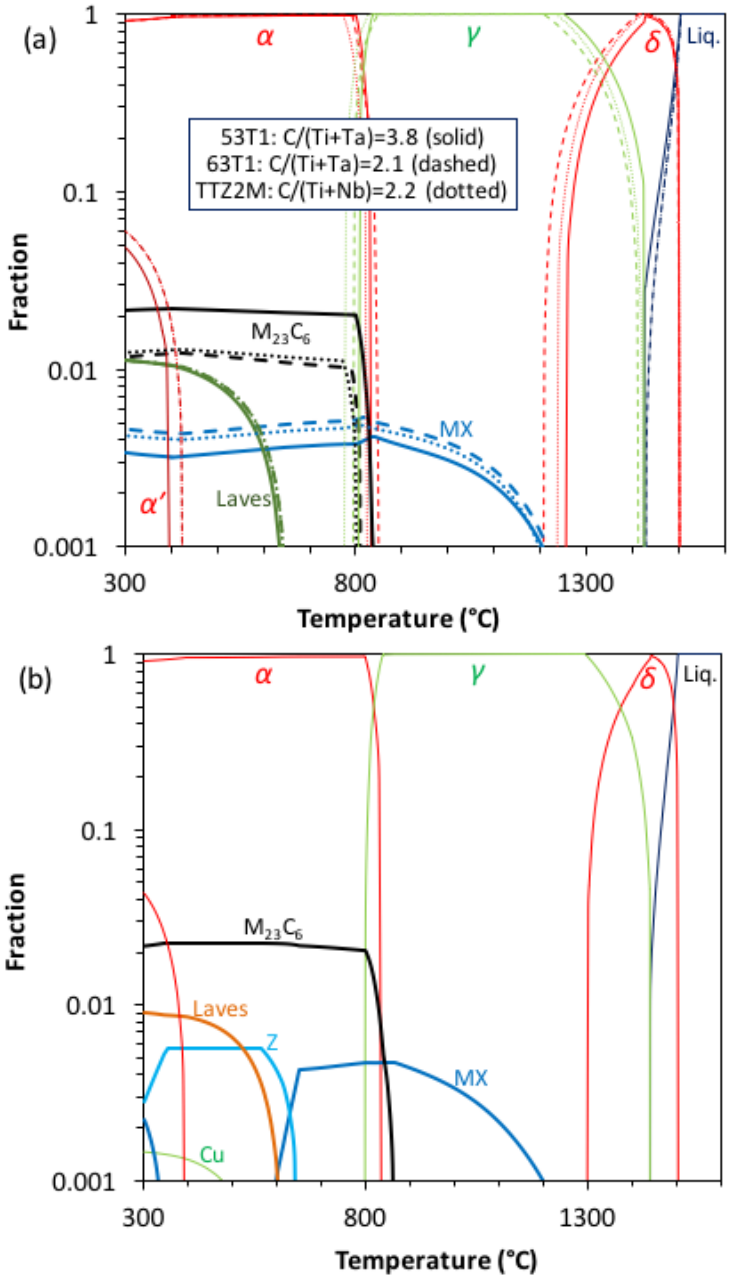

Figure 5. Calculated temperature-dependent phase fractions in 9Cr ferritic-martensitic steels of (a) the designed Fe-8.6Cr-1.3W-0.1tVTaTiC with a varied C/(Ti+Ta) atomic ratio of 3.8 (53T1, i.e., 91TT), 2.1 (63T1, i.e., 91TTa), and Fe-8.5Cr-1.3W-0.15Ti-0.1V-0.05Nb-0.1C with a C/(Ti+Nb) atomic ratio of 2.2 (TTZ2M), compared with (b) commercial Fe-8.4Cr-0.9Mo-0.22VNbCN (T91).

The designed ferritic and ferritic-martensitic steels with compositions in wt.% are listed in Table 1. The steels were arc-melted and drop cast in vacuum. Other than the four ferritic alloys Z3N4, Z3N7,

Z6N5, and Z6N9 in the as-cast condition, the other three ferritic alloys Z2N13, Z1N33A, and 2573 were solution-annealed at 1200°C for 10 min in argon atmosphere and hot-rolled at 1000°C with 75% thickness reduction, followed by air cooling. The Z1N33A was subjected to an aging at 650°C for 5 h, followed by air colling, to favor precipitates formation. In comparison, the ferritic-martensitic steels were subjected to an additional tempering process at 750°C for 2 h followed by air cooling, after solution annealing at 1130°C for 50 min in reducing atmosphere, followed by water quenching.

Table 1. Designed alloys to be screened.

Alloy ID	Nominal composition in wt% (with Fe balance)	Alloy type
Z3N4	12Cr-3Zr-3.3Ni	Ferritic
Z3N7	12Cr-3Zr-6.5Ni	Ferritic
Z6N5	12Cr-6Zr-4.5Ni	Ferritic
Z6N9	12Cr-6Zr-9Ni	Ferritic
Z2N13	12Cr-1.5Zr-1Ni-3W	Ferritic
Z1N33A	12Cr-1Zr-3Ni-3W-3Al	Ferritic
2573	15Cr-1.5W-1Mo-0.35Nb-0.15Ti-0.04C	Ferritic
53T1 (91TT)	8.6Cr-1.3W-0.1Ti-0.1Ta-0.13C	Ferritic-martensitic
63T1 (91TTa)	8.6Cr-1.3W-0.15Ti-0.1Ta-0.1C	Ferritic-martensitic
TTZ2M	8.5Cr-1.3W-0.15Ti-0.1V-0.05Nb-0.1C	Ferritic-martensitic

3. MICROSTRUCTURE CHARACTERIZATION

Three sets of samples were characterized, i.e., the Fe-rich Fe-Cr-Ni-Zr samples, the 12Cr Alloys Z2N13 and Z1N33A, and the 9Cr alloys 53T1 (91TT) and 63T1 (91TTa). The samples were mechanically polished for scanning electron microscopy (SEM) based characterizations using a JEOL 6500F and a Hitachi S4800, primarily in the backscattered electron (BSE) imaging mode, coupled with energy-dispersive X-ray spectroscopy (EDS). Both SEM have the field-emission gun (FEG) operated at acceleration voltages of 20 kV. X-ray diffraction (XRD) analysis was also conducted on some samples for phase identification, using a Bruker D2 phaser with Cu Kα radiation (λ=1.54056 Å) for a 2θ-scanning range of 30°–60° with a step size of 0.02° and 40 s diffraction collection time. Transmission electron microscopy (TEM) was used to characterize selected samples using a JEOL 2100F-FEG at 200 kV. Selected area electron diffraction (SAD) patterns were used to confirm the crystallography of the phases. Chemical composition analyses were investigated using TEM-based EDS, which has a significantly higher resolution than SEM-based EDS. TEM samples were prepared using focused-ion-beam (FIB) technique with a FEI versa 3D SEM/FIB dual beam system. A low voltage (e.g., 2 keV) ion-beam cleaning process was applied to the specimens as a final step to mitigate FIB-induced artifacts.

3.1 Effects of Nickel and Zirconium Content

Ferritic alloys Z3N4, Z3N7, Z6N5, and Z6N9 were designed to investigate the effects of Ni and Zr content on phase stability and mechanical properties. Two pieces were cut from each alloy, which were capsuled separately in evacuated quartz tubes and annealed at 1000 ºC for 336 h and 700 ºC for 1275 h, respectively. After the heat treatments, the samples were quenched in water to room temperature.

The SEM BSE images and EDS analyses were used to characterize the morphology and composition of the phases in the alloys. Figure 6 and 7 show the BSE images of the samples annealed at 700 ºC for 1275 hours and 1000 ºC for 336 hours, respectively. In both figures, the Fe-based matrix has a darker contrast while the intermetallic phases appear brighter because they contain Zr with a higher atomic mass. As shown in Figure 6, the samples annealed at 700 ºC have eutectic microstructures with features finer than 0.5 μm (for instance the inset of Figure 6c). Determined from the BSE images, the area fractions of the intermetallic phases are estimated to be 10 %, 13 %, 20 %, and 20 % for Z3N4, Z3N7, Z6N5, and Z6N9, respectively. Higher Zr content led to a higher fraction of intermetallic phases. As will be detailed later, EDS analyses show that all the characterized intermetallic phases are Zr rich.

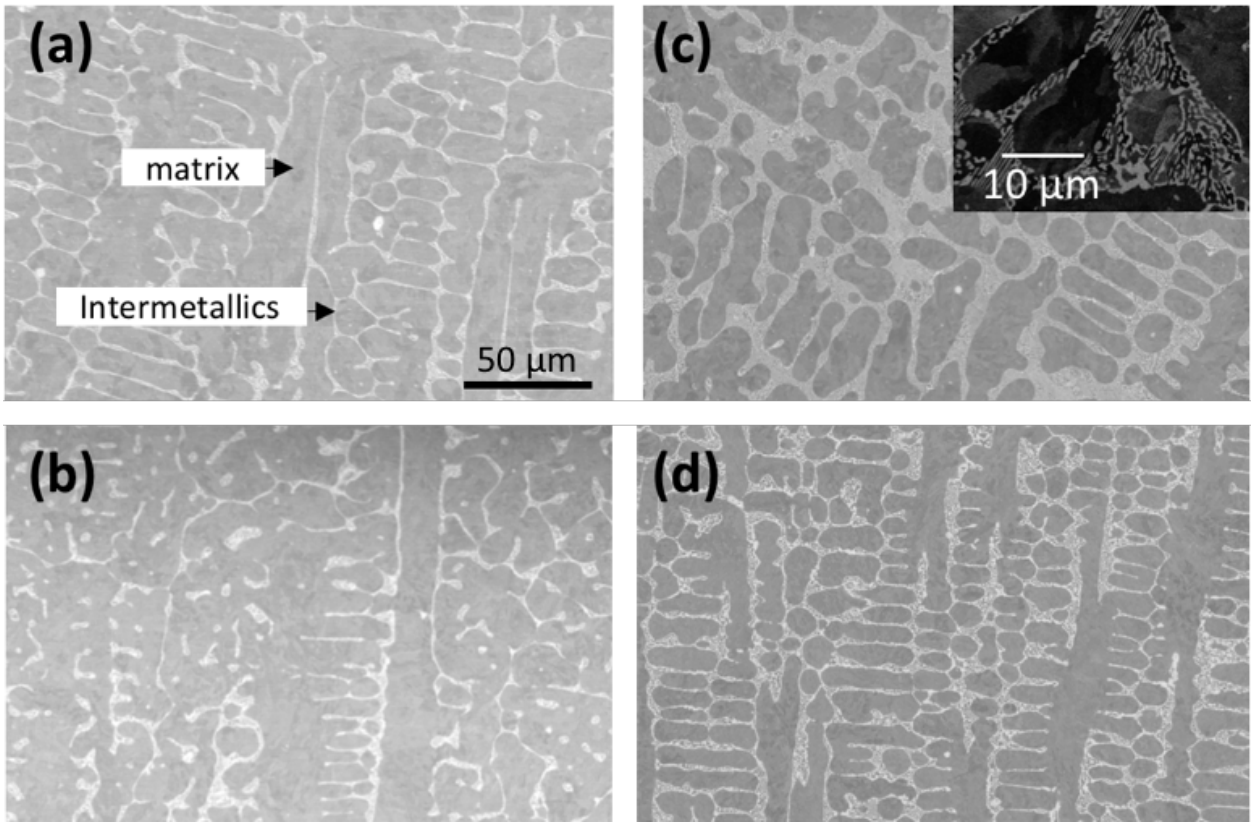

Figure 6. BSE images of the four samples, (a) Z3N4, (b)Z3N7, (c)Z6N5 and (d)Z6N9, annealed at 700 °C for 1275 hours.

In comparison with the micrographs of the samples annealed at 700 ºC for 1275 hours in Figure 6, no significant change of the overall fraction of the intermetallic phases were found after the 1000 °C aging for 336 hours in Figure 7. This suggests that the phase boundaries do not significantly change over the range of temperatures. However, the eutectic microstructures after annealed at 1000 ºC show coarser features than those at 700 ºC. This difference is demonstrated by the comparison between the inserts in Figure 6c and Figure 7d. This result suggests that the kinetics of the alloys at 700 ºC is not fast enough and the fine eutectic in the as-cast microstructure still remains after 1275-hour annealing. In contrast, coarsening due to the fast kinetics at 1000 ºC leads to a microstructural morphology more towards the equilibrium state. However, even for the samples annealed at 1000 ºC, fine features were still visible in Figure 7b and d, suggesting that global equilibrium was not fully reached even after the thermal annealing at 1000 ºC for 336 hours.

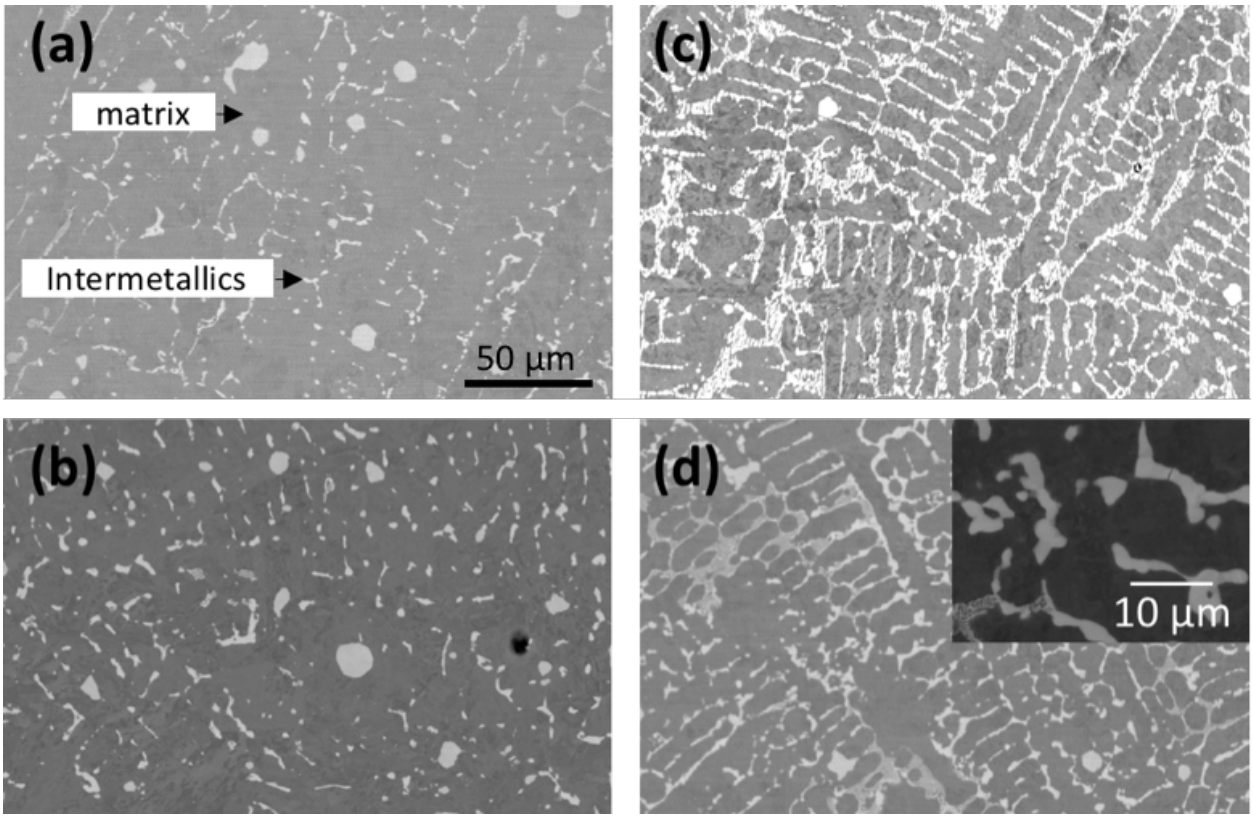

Figure 7. BSE images of the four samples, (a) Z3N4, (b)Z3N7, (c)Z6N5 and (d)Z6N9, annealed at 1000 °C for 336 hours.

The crystal structures of the phases in the four alloys were determined through XRD and TEM-based SAD. The XRD patterns of the samples annealed at 700 and 1000 ºC are shown in Figure 8a and b, respectively. The strongest peak near 2θ=44.56° corresponds to the (110) of body-centered-cubic (bcc) Fe-Cr matrix, to which the intensity of each pattern was normalized. The other labeled peaks are the (022) and (113) peaks of the C15_Laves phase and the (115) peak of the $Fe_{23}Zr_6$ phase with $Mn_{23}Th_6$-type crystal structure. The peaks of the C15_Laves and $Fe_{23}Zr_6$ phases were observed in all samples subjected to both annealing conditions, suggesting that both phases are stable at the temperature range of 700 - 1000 ºC. On the other hand, no peaks of the C14 or C36 types of Laves phase was observed in any of the samples at both annealing temperatures. A standard XRD pattern of LaB_6 overlapped with the Z6N9 pattern in Figure 8b was used to calibrate the 2θ measurements. Using the Bragg's formula, the lattice parameters of the C15_Laves phase and the $Fe_{23}Zr_6$ phase were calculated to be 0.698 and 1.169 nm, respectively.

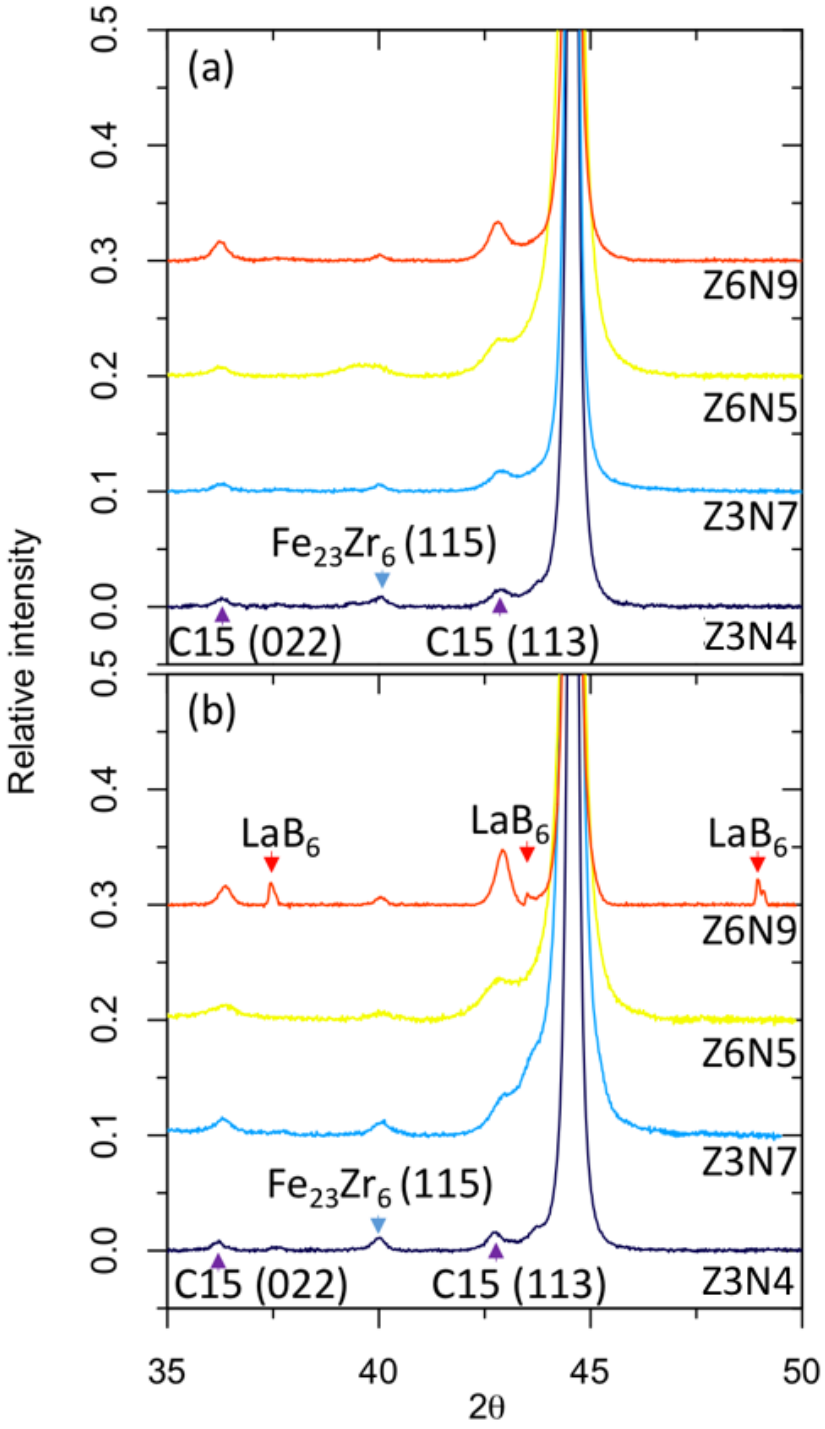

Figure 8. XRD patterns of the Z6N9, Z6N5, Z3N7 and Z3N4 samples annealed at (a) 700 °C for 1275 hours and (b) 1000 °C for 336 hours. LaB_6 was used as a standard.

The relative intensities of the peaks can be used to qualitatively estimate the fractions of the intermetallic phases listed in Table 2. The peaks of the intermetallic phases are systematically higher in the samples annealed at 1000 ºC compared to those annealed at 700 ºC because the intermetallic domains are

larger after annealing at 1000 ºC as shown in Figure 7. For both annealing temperatures, greater nickel content leads to a higher volume fraction ratio of C15_Laves to $Fe_{23}Zr_6$, as shown by comparison between the samples with similar Zr content but various Ni content (Z3N3 vs. Z3N7 and Z6N5 vs. Z6N9).

Table 2. Relative intensities of the Fe_2Zr_C15 (002) and $Fe_{23}Zr_6$ (115) peaks.

		C15 (%)	$Fe_{23}Zr_6$ (%)	C15 : $Fe_{23}Zr_6$
700 ºC	Z3N3	0.82	0.89	0.92
	Z3N7	0.73	0.63	1.15
	Z6N5	0.89	1.10	0.81
	Z6N9	1.69	0.55	3.05
1000 ºC	Z3N3	0.87	1.13	0.77
	Z3N7	1.56	1.30	1.20
	Z6N5	1.33	0.87	1.53
	Z6N9	1.66	0.69	2.41

In addition to the surveys with XRD, Figure 9 shows the results from TEM investigation of the Z3N7 sample annealed at 700 ºC for 1275 hours. Grains of ~0.5 μm in diameter were observed in the eutectic microstructure. Analysis of SAD patterns revealed that these grains with similar sizes have different crystal structures. Grain C was found to be the matrix phase, having a bcc crystal structure. The crystal structures of grains B and E are the C15 Laves structure and the $Mn_{23}Th_6$-type $Fe_{23}Zr_6$ structure, respectively. The observations of these two crystal structures agree with the XRD results. Grain D was found to have a Ni_7Zr_2_C12 structure, which was not distinguished from the XRD patterns in Figure 8 due to the small fraction of the Ni_7Zr_2 phase and the overlapping of the strongest peak of the Ni_7Zr_2 with the (110) peak of the matrix.

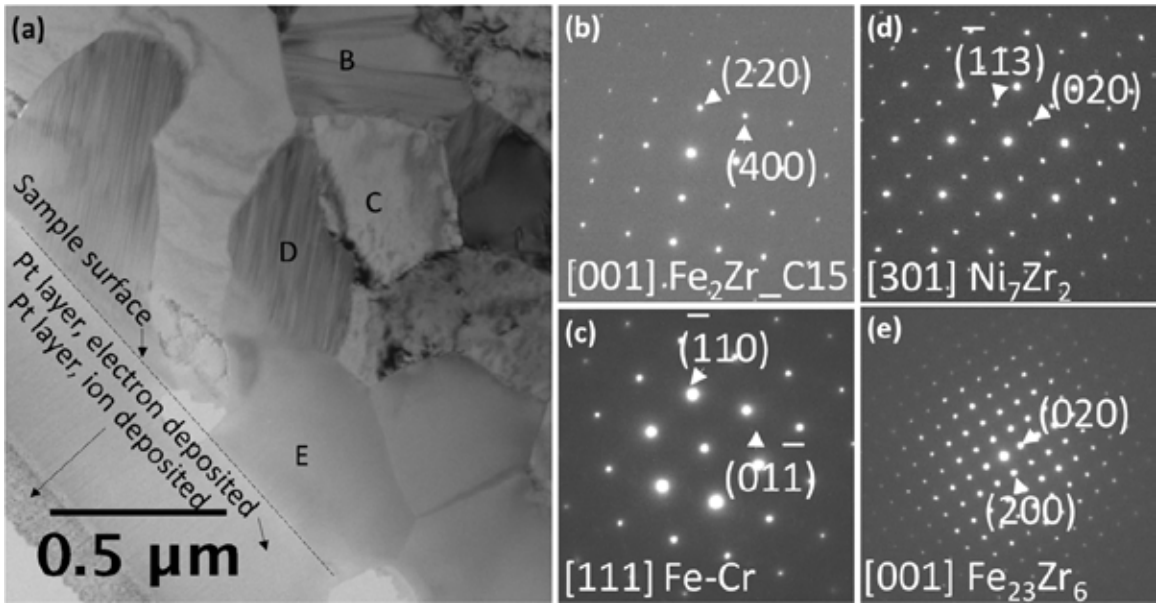

Figure 9. (a) A TEM bright-field image of the Z3N7 sample annealed at 700 °C for 1275 hours. (b-e) SAD patterns of the grains labeled as B-E in (a), respectively.

The chemical compositions of the labeled grains in Figure 9 were determined using TEM-based EDS technique. The averaged atomic percentages of Fe, Cr, Ni and Zr for each grain were listed in Table 3. The chemical compositions of the intermetallics in the Z3N7 sample annealed at 700 ºC show varied solubilities

of Ni in $(Fe,Ni)_2Zr$ as $(Fe_{0.74}Ni_{0.26})_2Zr$, Ni in $(Fe,Ni)_{23}Zr_6$ as $(Fe_{0.83}Ni_{0.17})_{23}Zr_6$, and Fe in $(Ni,Fe)_7Zr_2$ as $(Ni_{0.50}Fe_{0.50})_7Zr_2$.

Table 3. Chemical compositions of different phases in the Z3N7 sample annealed at 700 ºC for 1275 hours surveyed by EDS with TEM (atomic %).

	Matrix	$(Fe,Ni)_2Zr$	$(Fe,Ni)_{23}Zr_6$	$(Ni,Fe)_7Zr_2$
Fe	84.59 ± 0.16	49.82 ± 2.36	62.67 ± 0.33	37.43 ± 2.00
Cr	13.79 ± 0.37	1.49 ± 0.18	4.01 ± 0.10	0.91 ± 0.24
Ni	1.49 ± 0.09	17.49 ± 0.31	12.96 ± 0.55	37.05 ± 0.35
Zr	0.12 ± 0.25	31.20 ± 2.84	20.37 ± 0.78	24.63 ± 1.89

A more systematically study of the chemical compositions of all the samples were conducted using EDS on SEM. Figure 10 shows the EDS mappings of the Z6N5 sample annealed at 700 ºC and the Z3N7 samples annealed at 700 and 1000 ºC in columns a-c, respectively. The elemental distributions of Fe, Cr, Ni and Zr were obtained using FeK, CrK, NiK and ZrL peaks. Overall, the intermetallic phases are rich in Zr and Ni, while the matrix phase is rich in Fe and Cr and lean in Zr and Ni. Ni and Zr are not uniformly distributed in the intermetallics, as seen in Figure 10b. Particularly, in Z3N7 and Z6N9 samples annealed at 700 ºC, the presence of a Ni-concentrated intermetallic was frequently observed. None of the Ni-concentrated phase was observed in the sample of Z6N5, which has the lowest ratio of Ni to Zr. Qualitatively, the fraction of the Ni-dominant phase is correlated to the ratio of the compositions of Ni and Zr rather than the absolute compositions of Zr or Ni. After annealed at 1000 ºC, the Ni-dominant phase disappeared from the intermetallics. An example of the Z3N7 sample annealed at 1000 ºC is shown in Figure 10c.

Table 4 summaries the atomic percentages of the matrix and intermetallics determined by EDS on SEM of the samples annealed at 700 and 1000 ºC, respectively. Given that the interaction volume for the X-ray is on the order of 1 μm, the chemical compositions of the intermetallics are inevitably influenced by the surrounding matrix, resulting to overestimation of Fe and Cr and underestimation of Ni and Zr in the intermetallics, as shown by comparison between Table 3 and 4. Still, the three intermetallics, namely, $(Fe,Ni)_2Zr$, $(Fe,Ni)_{23}Zr_6$ and $(Ni,Fe)_7Zr_2$, are distinctive by the Fe:Ni:Zr ratio. In Figure 10, the Ni concentrated regions correspond to $(Ni,Fe)_7Zr_2$, which is only observed in the Z3N7 and Z6N9 samples annealed at 700 ºC. The finding of Ni_7Zr_2 which is more stable at low temperature and has high Ni content is consistent with the recent study in the Fe-Ni-Zr system [16]. The rest Ni and Zr rich domains correspond to either $(Fe,Ni)_2Zr$ or $(Fe,Ni)_{23}Zr_6$, which were observed in all the samples of both annealing temperatures. In addition, as shown in Figure 7, $(Fe,Ni)_{23}Zr_6$ appeared having a patchy structure with a diameter on the order of 10 μm in the samples annealed at 1000 º C, agreeing to the morphology of $Fe_{23}Zr_6$ observed in Fe-Zr binary systems [17]. The intermetallics observed in the samples annealed at 700 ºC did not show such morphological characteristics.

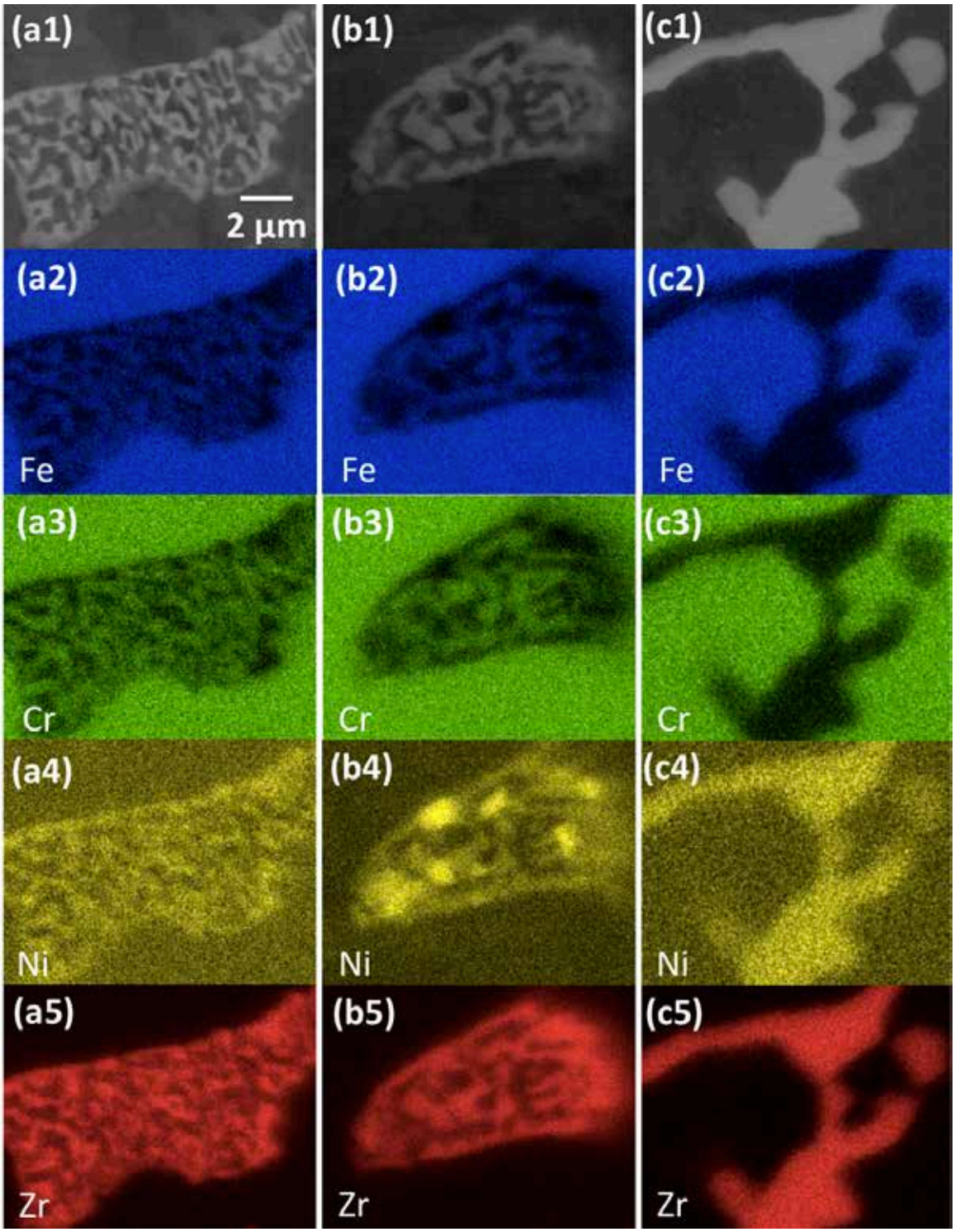

Figure 10. The EDS mappings of (a) the Z6N5 sample annealed at 700 ºC and (b-c) the Z3N7 samples annealed at 700 and 1000 ºC, respectively, using FeK, CrK, NiK and ZrL peaks.

Table 4. Chemical compositions of samples annealed at 700 ºC for 1275 hours and 1000 ºC for 336 hours surveyed by EDS with SEM (atomic %).

		700 ºC annealed for 1275 hours				1000 ºC annealed for 336 hours		
		Matrix	$(Fe,Ni)_2Zr$	$(Fe,Ni)_{23}Zr_6$	$(Ni,Fe)_7Zr_2$	Matrix	$(Fe,Ni)_2Zr$	$(Fe,Ni)_{23}Zr_6$
Z	Fe	84.59 ± 0.17	58.95 ± 0.20	68.06 ± 1.17	-	83.39 ± 0.21	63.30 ± 0.64	68.12 ± 0.29
3	Cr	13.58 ± 0.07	5.27 ± 0.43	7.92 ± 0.65		13.77 ± 0.10	5.11 ± 0.30	7.39 ± 0.68
N	Ni	1.41 ± 0.14	13.25 ± 0.45	7.97 ± 0.83		2.56 ± 0.09	5.83 ± 0.10	4.71 ± 0.13
3	Zr	0.42 ± 0.05	22.54 ± 0.31	16.04 ± 0.70		0.28 ± 0.15	25.77 ± 0.77	19.79 ± 1.06
Z	Fe	80.36 ± 0.26	58.30 ± 1.16	64.41 ± 0.46	54.47 ± 2.32	80.72 ± 0.17	55.58 ± 0.68	64.32 ± 0.66
3	Cr	13.99 ± 0.11	5.86 ± 1.07	8.39 ± 0.20	6.53 ± 0.19	14.03 ± 0.03	4.32 ± 0.30	7.65 ± 0.21
N	Ni	5.08 ± 0.19	13.65 ± 0.85	10.93 ± 0.57	23.69 ± 0.99	5.05 ± 0.23	12.94 ± 0.49	8.70 ± 0.34
7	Zr	0.56 ± 0.19	21.74 ± 1.52	16.26 ± 0.70	15.31 ± 1.49	0.21 ± 0.05	27.16 ± 0.59	19.33 ± 0.10
Z	Fe	81.78 ± 0.18	63.66 ± 0.76	67.61 ± 1.31	-	81.76 ± 0.10	60.64 ± 0.68	66.21 ± 0.65
6	Cr	14.26 ± 0.20	6.97 ± 0.26	9.21 ± 0.48		14.92 ± 0.12	5.14 ± 0.67	7.58 ± 0.49
N	Ni	3.55 ± 0.47	9.00 ± 0.34	7.33 ± 0.84		3.06 ± 0.15	8.19 ± 0.32	5.68 ± 0.31
5	Zr	0.41 ± 0.16	20.36 ± 0.75	15.85 ± 1.12		0.26 ± 0.05	26.02 ± 1.03	20.54 ± 1.00
Z	Fe	78.37 ± 0.79	55.16 ± 1.20	65.03 ± 0.72	49.35 ± 2.39	78.27 ± 0.43	52.30 ± 0.11	59.89 ± 0.37
6	Cr	14.81 ± 0.06	5.09 ± 0.76	9.40 ± 0.53	6.01 ± 1.30	14.81 ± 0.05	4.33 ± 0.20	6.86 ± 0.11
N	Ni	6.06 ± 0.55	16.4 ± 0.60	11.41 ± 0.81	27.14 ± 1.51	6.74 ± 0.25	18.11 ± 0.16	12.05 ± 0.38
9	Zr	0.58 ± 0.04	23.25 ± 1.75	16.16 ± 1.30	17.44 ± 2.25	0.27 ± 0.15	25.25 ± 0.14	21.20 ± 0.11

The Laves phase $(Fe,Ni)_2Zr$ in this study was observed to have a cubic C15 structure regardless of the alloy compositions or annealing temperatures. Neither of the hexagonal structure s of C14 or C36 was observed. In Fe-Zr binary system, the C15 is the stable phase up to the melting point near the stoichiometric composition and the C36 is found as a high-temperature phase between 1240 and 1345 ºC with a Zr concentration lower than that of the C15. While the hexagonal C14 is not stable in Fe-Zr binary system, it is stabilized by Cr in Fe-Cr-Zr ternary system by geometric factors [18]. In this study, there is more Ni replaces Fe in the Laves phase than Cr does. Consequently, the C15 structure is promoted by Ni over the C14 hexagonal structures for the Laves phase, probably favored by altering the electron concentration factor as suggested in Ref. [19]. The roles of Ni and Cr in stabilizing different structures of Laves phase was also illustrated by previous studies of alloys composed of 304/316SS and Zr, where higher Cr/Ni ratio favors the C14 structure, followed by C36 and then C15 [19].

The $(Fe,Ni)_{23}Zr_6$ phase has been observed in the Fe-Zr binary and Fe-Cr-Zr ternary systems as well as alloys composed of SS 304/316 and Zr [20]. Stein et. al reported that the $Fe_{23}Zr_6$ in the Fe-Zr binary system was associated with an increased oxygen-concentration and concluded that the $Fe_{23}Zr_6$ phase was oxygen-stabilized [20]. Our EDS analysis did not show elevated oxygen content in $Fe_{23}Zr_6$. The stability of $Fe_{23}Zr_6$ was recently investigated by Yang et. al through a combined effort of thermodynamics calculations and experiments. They reported that Gibbs energy difference for the Fe-20.69 at% Zr alloy (stoichiometric composition of $Fe_{23}Zr_6$) with and without the $Fe_{23}Zr_6$ phase being stable is negligible, suggesting that $(Fe,Cr)_{23}Zr_6$ phase can easily become stable due to impurities or some kinetic factors, if it is not a stable phase [21]. $Fe_{23}Zr_6$ was found to be stable in a recent study on the phase equilibrium in the Fe-Ni-Zr system [16]. In the current study, $Fe_{23}Zr_6$ was found to be stable under the 700 and 1000 º C annealed conditions.

To better visualize the phase relationship, analogs to the Fe-Ni-Zr ternary phase diagram showing the tie-triangles of bcc, Fe_2Zr_C15, $Fe_{23}Zr_6$ in Z3N3, Z3N7, Z6N5, and Z6N9 at 700 and 1000 ºC are plotted in Figure 11a and b, respectively. The three phases were distinguished by the sizes of the solid symbols, with the small, middle and big symbols representing bcc, $Fe_{23}Zr_6$ and Fe_2Zr, respectively. The tie-triangles in these figures are based on the data from Table 4 with the Cr content being combined with the Fe content. Despite the measurement uncertainties of the SEM/EDS, important information can be obtained. Firstly, the Zr content in the intermetallic phases are more towards the stoichiometric compositions at the high

temperature, suggesting that the high temperature data are more towards equilibrium. Secondly, the Ni content in the C15 Laves phase is more than that in $Fe_{23}Zr_6$, suggesting that Ni addition favors the formation of the C15 Laves phase over $(Fe,Ni)_{23}Zr_6$, as supported by the XRD results shown in Table 2. Thirdly, the width of all tie-triangles at a fixed Zr content are narrow. The second and third findings are in agreement with the recently reported Fe-Ni-Zr isothermal section [16]. In addition to phase compositions, the bulk compositions of the four alloys, which were determined using SEM/EDS and listed in Table 5, are plotted in Figure 11a and b as hollow symbols. Compared to the nominal alloy compositions, these values consistently show increased Zr and decreased Ni, indicating the Zr segregation in these regions. Except for the Z6N5 alloy, all bulk compositions are located within or close to the tie-triangles, satisfying the mass balance of element partition. Based on phase rule, for a four-component system, when temperature, pressure and concentrations of two components are fixed, a three-phase equilibrium can be uniquely defined. Therefore, we should anticipate that Z3N3 and Z3N7 are in the same three phase equilibrium and Z6N5 and Z6N9 are in the same equilibrium. However, the measured tie-triangles of Z3N3 and Z3N7 do not overlap with each other, neither for those of Z6N5 and Z6N9. This analysis suggests that not all of the four alloy compositions are in true thermodynamics phase equilibrium of bcc + $Fe_{23}Zr_6$ + Fe_2Zr_C15. Then why are all the three phases present in all samples? The explanation, which is detailed in the following paragraph, is that the coexistence of bcc + $Fe_{23}Zr_6$ + Fe_2Zr_C15 in some samples does not represent a three-phase equilibrium, but a result of the competitive thermodynamics and kinetics of the formations of $Fe_{23}Zr_6$ and Fe_2Zr_C15.

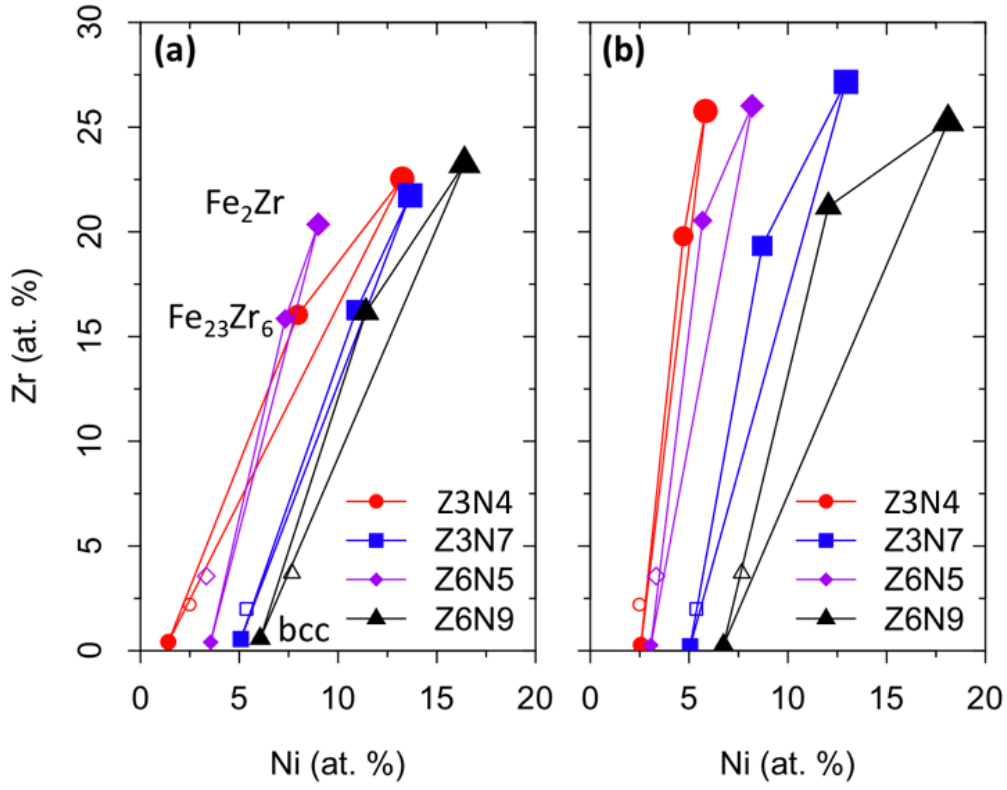

Figure 11. Analogs to the Fe-Ni-Zr ternary phase diagram showing the phase compositions of bcc, Fe_2Zr_C15, $Fe_{23}Zr_6$ in Z3N4, Z3N7, Z6N5, and Z6N9 at (a) 700 and (b) 1000 °C. The phases were distinguished by the sizes of the solid symbols, with the small, middle and big symbols representing bcc, $Fe_{23}Zr_6$ and Fe_2Zr, respectively. The hollow symbols represent the chemical compositions of the alloys.

Table 5. Chemical compositions of the Fe-Cr-Ni-Zr alloys surveyed by SEM/EDS (atomic %).

	Fe	Cr	Ni	Zr
Z3N3	82.20 ± 0.28	13.12 ± 0.22	2.49 ± 0.24	2.21 ± 0.17
Z3N7	79.41 ± 0.73	13.11 ± 0.12	5.37 ± 0.37	2.00 ± 0.25
Z6N5	79.69 ± 0.11	13.42 ± 0.16	3.33 ± 0.30	3.57 ± 0.04
Z6N9	75.23 ± 1.06	13.41 ± 0.07	7.67 ± 0.66	3.71 ± 0.34

Yang et al. has calculated the Fe-Zr binary phase diagram with and without $Fe_{23}Zr_6$. The one with $Fe_{23}Zr_6$ is shown in Figure 12 [22]. It shows that for Fe-rich Fe-Zr alloys with Zr up to 10 at. %, the Fe_2Zr_H, i.e., the Fe_2Zr_C36 Laves phase, forms during eutectic solidification. This phase participates two solid-state phase transformations. One is the peritectoid reaction of Fe_2Zr_C36 + fcc → $Fe_{23}Zr_6$. If this reaction is complete, all Fe_2Zr_C36 would be consumed and the final microstructure would be fcc+ $Fe_{23}Zr_6$. The fcc will transform to bcc during cooling. Therefore, we will eventually get a microstructure of bcc+ $Fe_{23}Zr_6$. However, the peritectoid reaction is kinetically unfavorable. The formation of $Fe_{23}Zr_6$ will serve as a diffusion barrier between the fcc and the $Fe_{23}Zr_6$ and slow down the transformation kinetics. On the other hand, because Fe_2Zr_C36 has a composition very close to that of Fe_2Zr_C15 (labeled as Fe_2Zr_C in Figure 12), it is kinetically favorable to directly transform to Fe_2Zr_C15, especially considering that the thermodynamic driving force for Fe_2Zr_C15 is only slightly less than that of $Fe_{23}Zr_6$ [22]. At lower temperatures, the peritectoid reaction is even more sluggish, and thus less $Fe_{23}Zr_6$ can form. In the Fe-Cr-Ni-Zr quaternary, the Fe_2Zr_C15 is stabilized over the Fe_2Zr_C36, therefore, a primary solidification region of is expected, leading to direct formation of Fe_2Zr_C15 from liquid. If the kinetics is fast enough, some Fe_2Zr_C15 would transform to $Fe_{23}Zr_6$ through the peritectoid reaction of Fe_2Zr_C15 + fcc → $Fe_{23}Zr_6$. However, the slow kinetics of peritectoid reaction greatly limits this transformation. On the other hand, keeping in mind the eutectic temperature of Liquid→ Fe_2Zr_C36+fcc is slightly higher than the peritectoid temperature of fcc+Fe_2Zr_C36 → $Fe_{23}Zr_6$ in Figure 12. The stabilizing effect of Ni on $Fe_{23}Zr_6$ may lead to a small primary solidification region. Therefore, some $Fe_{23}Zr_6$ may form directly from liquid. In summary, for Fe-rich Fe-Cr-Ni-Zr alloys, $Fe_{23}Zr_6$ and Fe_2Zr_C15 are thermodynamically competing phases. The formation of Fe_2Zr_C15 is mainly from solidification. $Fe_{23}Zr_6$ is a thermodynamically stable phase. Its formation can either through direct solidification from liquid or peritectoid transformation from Fe_2Zr_C15 with rather limited kinetics.

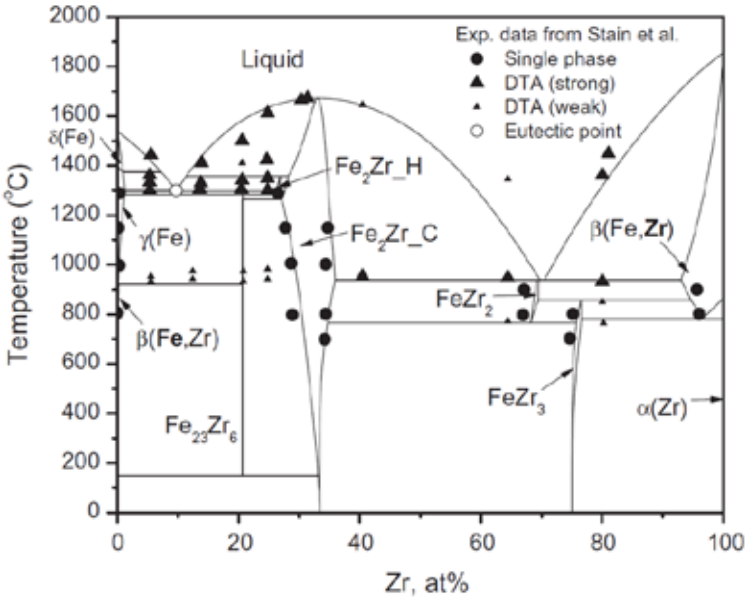

Figure 12. Calculated Fe-Zr phase diagram with the stable $Fe_{23}Zr_6$ phase replotted from Ref. [22]

3.2 Microstructures of The 12Cr Alloys Z2N13 and Z1N33A

Figure 13 shows the optical images of the 12Cr ferritic alloys Z2N13 and Z1N33A and 15Cr alloy 2573. Some coarse Laves particles in dark grey formed in short strings in Z2N13 and Z1N33A, which are likely to be primarily C15_Laves with some C14_Laves as suggested by Figure 4b-c. In contrast to Z2N13, a high density of fine particles formed in Z1N33A. Alloy 2573 shows a high density of fine Laves phase particles, together with a few discrete coarse particles, which was developed in a previous project. It is included in the ion irradiation screening study to check the amorpharization tendency of the fine Laves phase.

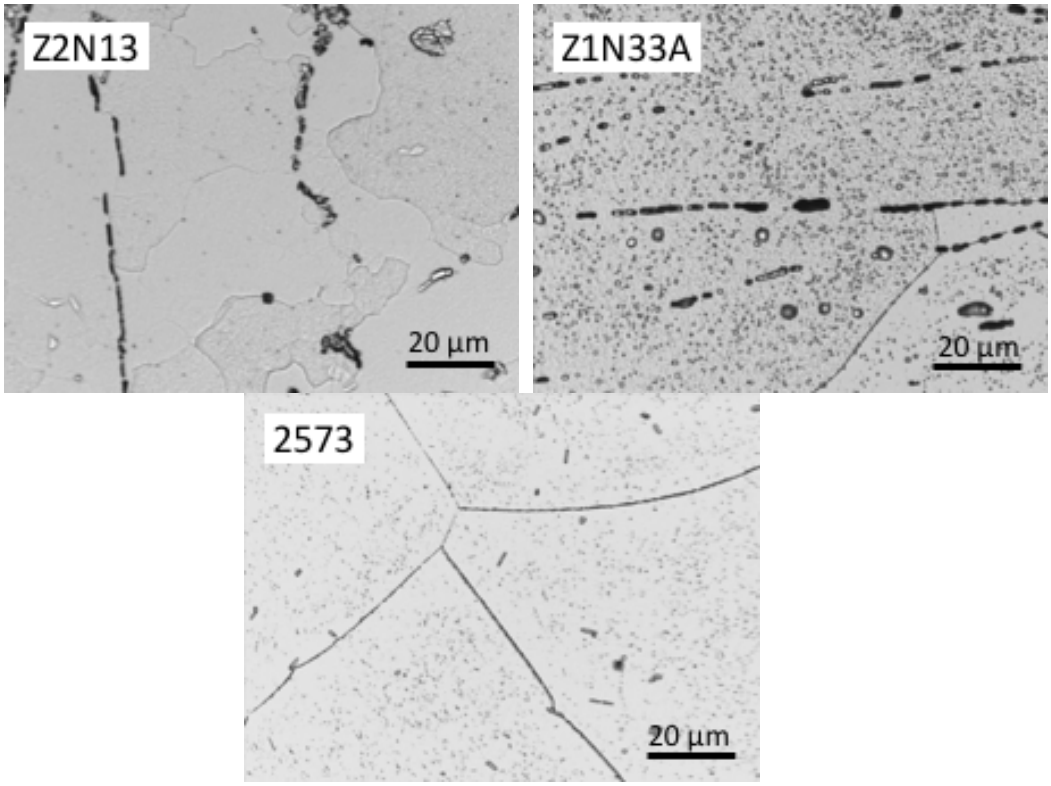

Figure 13. Optical images of the 12Cr alloys Z2N13 and Z1N33A and 15Cr alloy 2573.

Figure 14 and 15 show the BSE images of the Z2N13 and Z1N33A samples. The low magnification micrograph of Z2N13 in Figure 14a shows the intermetallics with bright contrast decorating the matrix that has dark contrast, particularly on the grain boundaries. The BSE contrast suggests 10–20 µm grain size of Z2N13, which is consistent with the optical image result in Figure 13. As shown in Figure 14b, the intermetallics have a typical size of 1 µm. The average results from the EDS point surveys at domains labeled by numbers in Figure 14b are listed in Table 6. The intermetallic phase is likely to $(Fe, Ni)_2Zr$ based on its chemical composition. Figure 15 shows BSE micrographs from the Z1N33A sample. Similar to the Z2N13 sample, intermetallics approximately decorating the grain boundaries were also observed as shown in Figure 15a. The average results from the EDS point surveys carried out at the number-labeled domains in Figure 15b are listed in Table 7. In addition to the Zr-rich intermetallics, dispersive nanoparticles were observed in the matrix, as shown in the high-magnification BSE images of Figure 15c-d. Due to the resolution limit of SEM/EDS, the composition of the ultrafine particles cannot be revealed. Yet, the dark

contrast of the particles indicates that the particles are composed of elements with less atomic mass than the averaged atomic mass of the matrix.

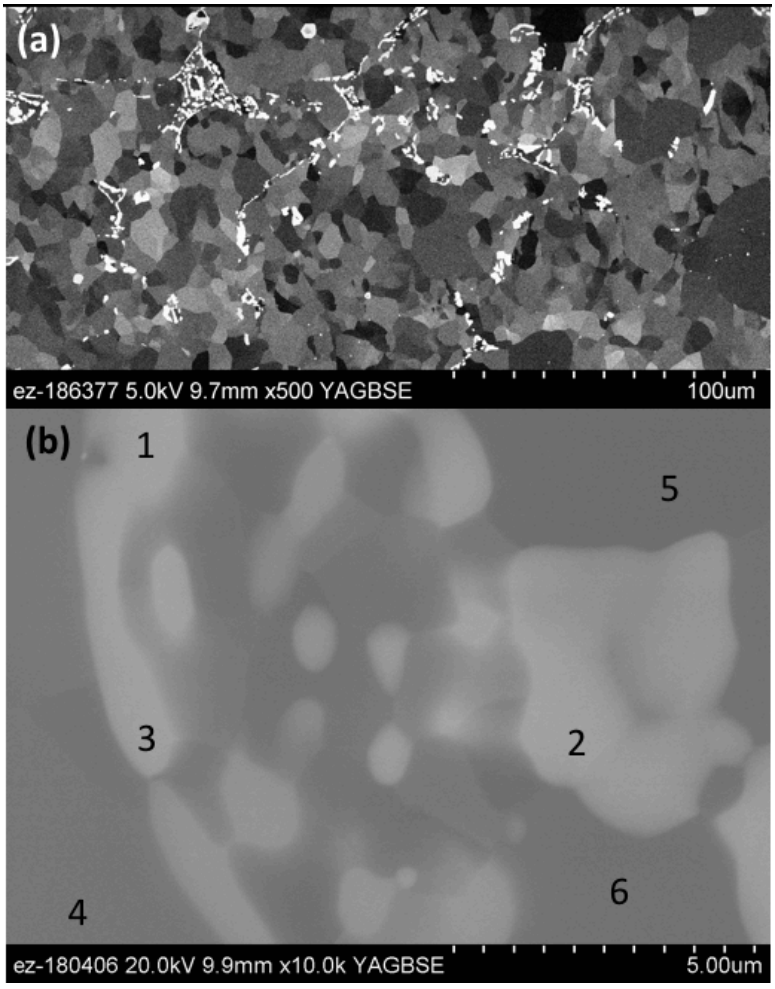

Figure 14. BSE images of the Z2N13 sample.

Table 6. Phase composition in Z2N13 surveyed by EDS with SEM (atomic %).

	Fe	Cr	Ni	Zr	W
Intermetallic	66.63 ± 0.30	6.45 ± 0.18	2.90 ± 0.14	22.29 ± 0.34	1.72 ± 0.05
Matrix	83.87 ± 0.01	13.95 ± 0.20	0.57 ± 0.08	0.57 ± 0.06	1.06 ± 0.06

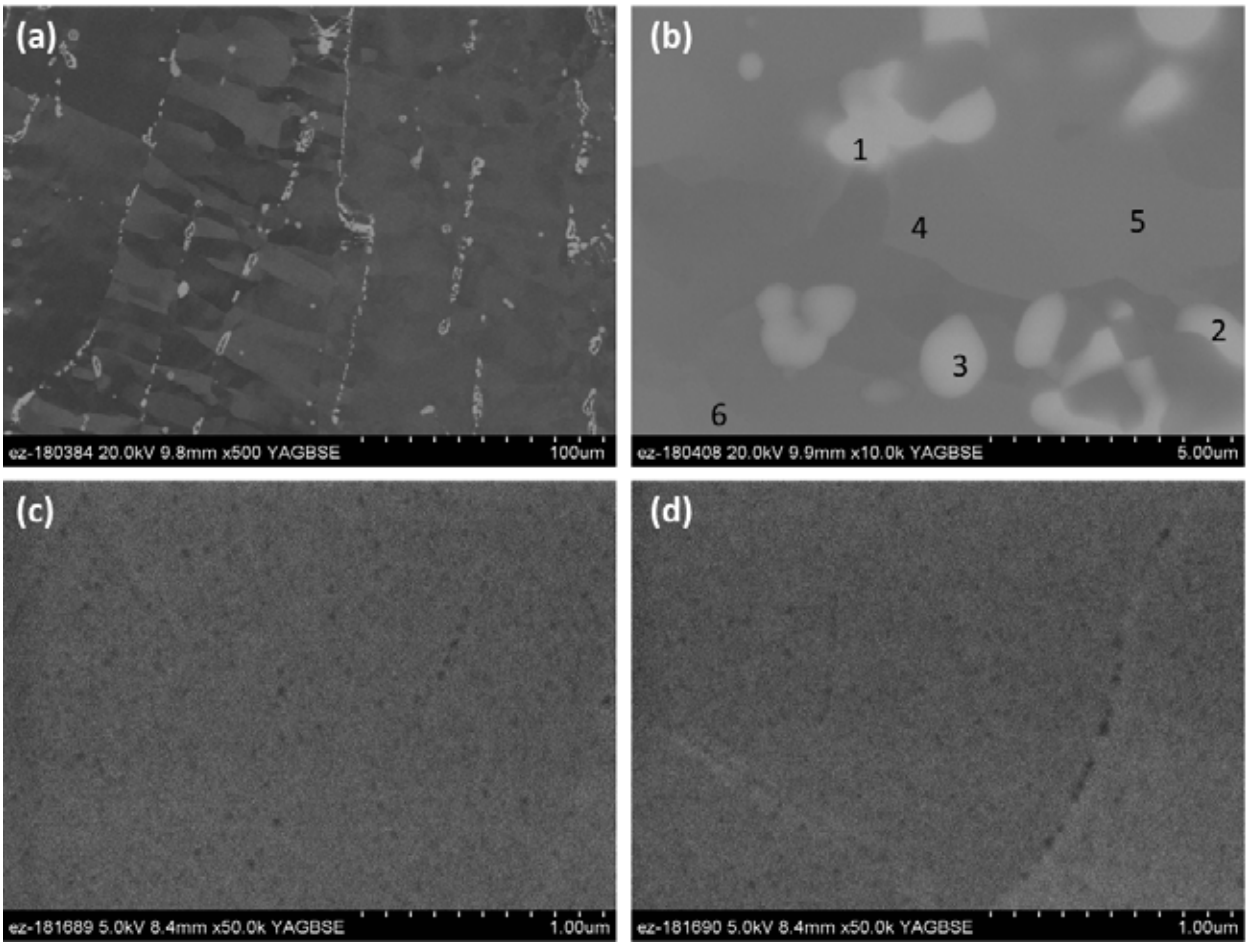

Figure 15. BSE images of the Z1N33A sample.

Table 7. Phase composition in Z1N33A surveyed by EDS with SEM (atomic %).

	Fe	Cr	Ni	Zr	W	Al
Intermetallic	60.97±2.02	7.46±1.26	6.65±1.02	17.33±1.89	2.05±1.42	5.46±1.76
Matrix	76.41±0.20	12.96±0.36	2.46±0.06	0.33±0.12	1.84±1.13	5.79±1.69

TEM specimens of Z1N33A were prepared using FIB. Figure 16a shows a high-angle annular dark-field (HAADF) image of the specimen having intermetallics decorating some of the boundaries. The SAD pattern of the intermetallics in Figure 16b suggests the C14 hexagonal structure of Laves phase. In the bcc matrix, we observed many nanoparticles, as shown in Figure 16c. A SAD pattern of the matrix containing the nanoparticles are shown in Figure 16d, which shows coherent relationship between the bcc matrix and the nanoparticles in a B2 structure. The mean diameter and density of the nanoparticles were measured to be 11.3 ± 1.9 nm and (1.36 ± 0.23) × 10^{22} m^{-3}, respectively.

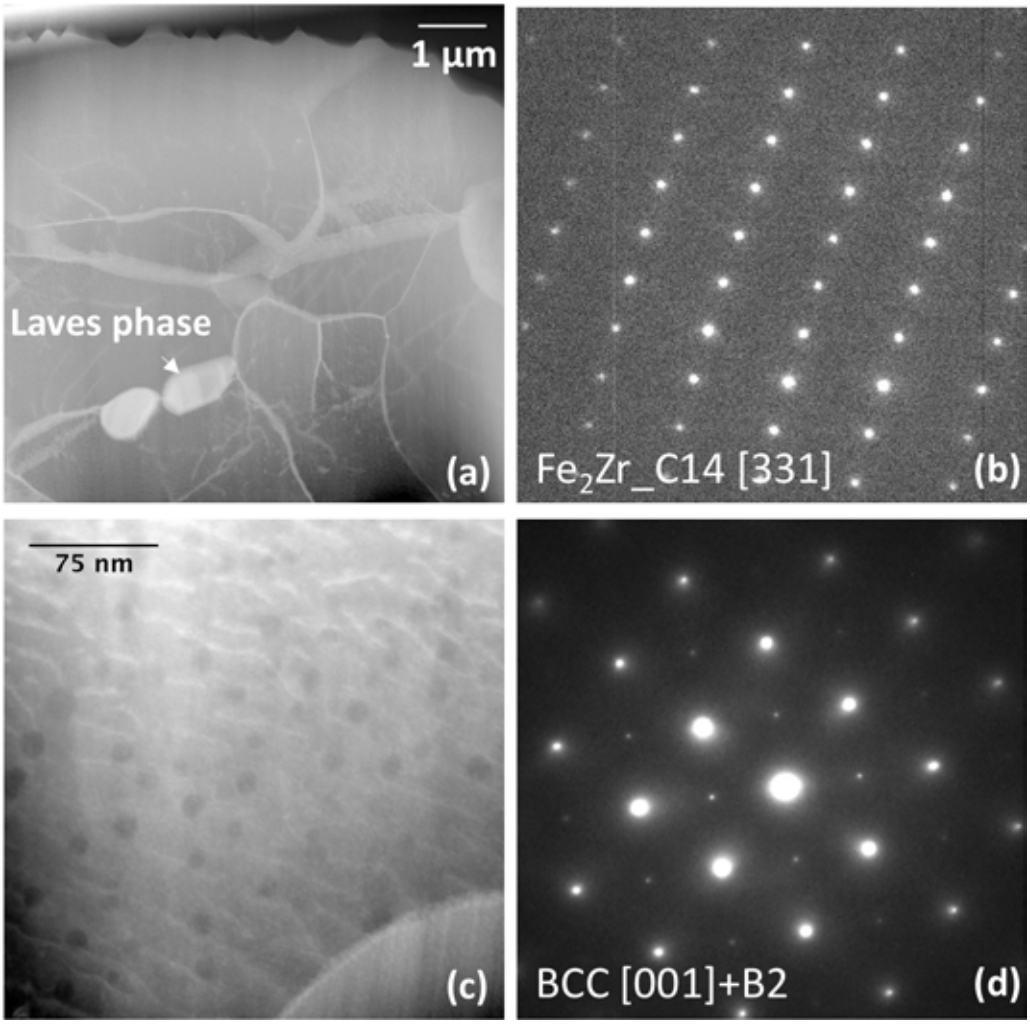

Figure 16. (a) Low-magnification HAADF micrograph showing the microstructure of the Z1N33A. (b) A SAD pattern from the intermetallic phase in (a). (c) High-magnification HAADF micrograph showing the nanoparticles. (d) A SAD pattern from the matrix containing the nanoparticles.

Figure 17 shows the results of EDS mapping of a nanoparticle. Compared to the surrounding matrix, the particles are Ni and Al rich. Considering that the crystal structure of the nanoparticle is B2, as shown in Figure 16d, the nanoparticles are likely to be NiAl. Quantitatively, the chemical compositions of the BCC matrix, Laves phase and nanoparticles determined by EDS are listed in Table 8. The accuracy of TEM-based EDS is expected to be better than that from SEM/EDS due to the improved resolution. Although nanoparticles are still too small to get their compositions measured accurately, the ratio of Al and Ni shows agreement to the stoichiometry of the B2 NiAl phase.

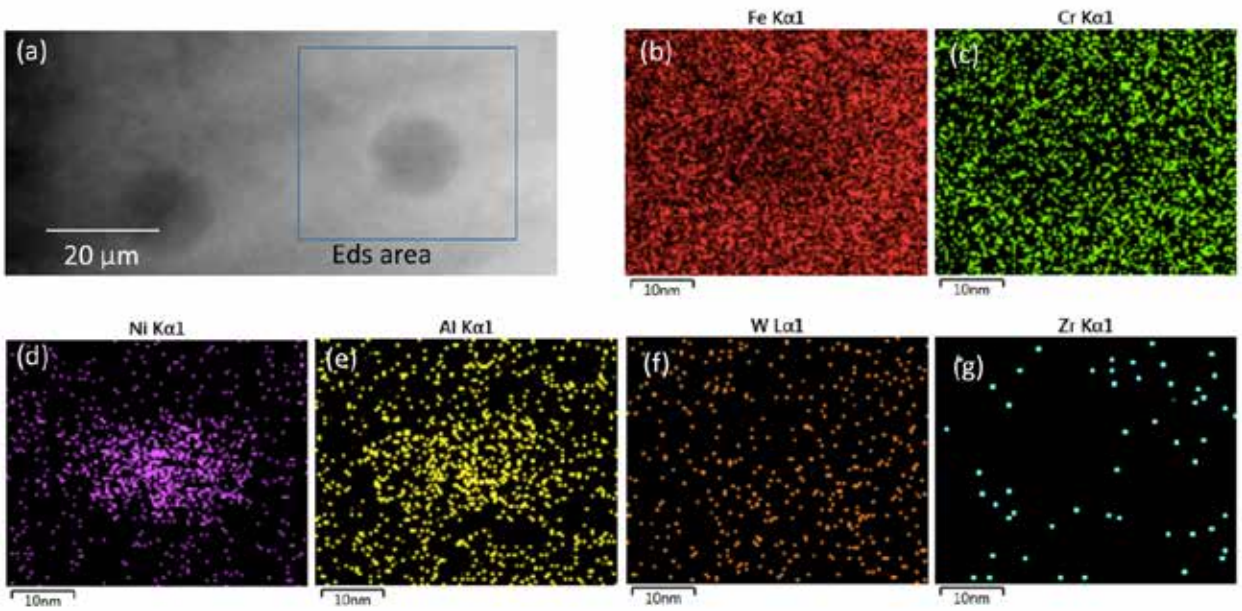

Figure 17. (a) A HAADF image showing the nanoparticle surveyed by EDS mapping. (b-g) EDS mapping of Fe, Cr, Ni, Al, W, Zr, respectively.

Table 8. Chemical compositions of the bcc matrix, Laves phase and nanoparticles in Z1N33A surveyed by EDS with TEM (atomic %).

	Fe	Cr	Ni	Zr	W	Al
Matrix	69.93 ± 2.07	5.91 ± 0.60	5.41 ± 1.83	0.15 ± 0.23	18.22 ± 2.87	0.38 ± 0.23
Laves	45.15 ± 2.53	1.13 ± 0.14	12.66 ± 0.53	28.55 ± 2.37	12.28 ± 4.38	0.22 ± 0.16
Nanoparticle	53.96 ± 2.88	8.56 ± 1.17	15.27 ± 2.10	0.00 ± 0.01	4.98 ± 2.35	17.22 ± 1.22

3.3 Microstructures of The 9Cr Alloys 53T1 (91TT) and 63T1 (91TTa)

The optical micrographs of the 9Cr ferritic-martensitic steels 53T1 (91TT) and 63T1 (91TTa) are shown in Figure 18a-d. Two types of etchants were used on the polished samples. The solution of $50H_2O/5HNO_3/1HF$ revealed clear lath and boundary structures as shown in the left column, which indicate that the steels are primarily composed of tempered martensite microstructure. Some retained delta-ferrite was observed in 91TTa, which seems more pronounced than that in 91TT. The other etchant of 10g oxalic acid in 100 ml distilled water primarily revealed particles in the samples as shown in the right column, which are mainly $M_{23}C_6$ particles according to the resolution of optical microscopy. It seems that 91TT contains a finer structure with more particles than 91TTa, qualitatively consistent with the thermodynamic calculations as shown in Figure 5. The high-resolution SEM BSE images of 91TT and 91TTa in Figure 19 show the presence of many ultrafine particles in white, suggesting Ta-rich (high atomic weight) MX-type precipitates. It seems that 91TTa has less Ta-rich particles than 91TT, which may be due to the presence of higher Ti content in 91TTa, increasing the competition of the formation of TiC-type MX precipitates. TEM characterization will be conducted to identify the presence of Ti-rich carbides. The optical micrograph of 9Cr TTZ2M is included in Figure 18e for comparison, which was developed in a previous project and exhibited superior properties in the 9Cr steel category. Compared to the 53T1 and 63T1, the optical micrograph of TTZ2M did not show obvious retained delta-ferrite, but somewhat coarser block/lath structures.

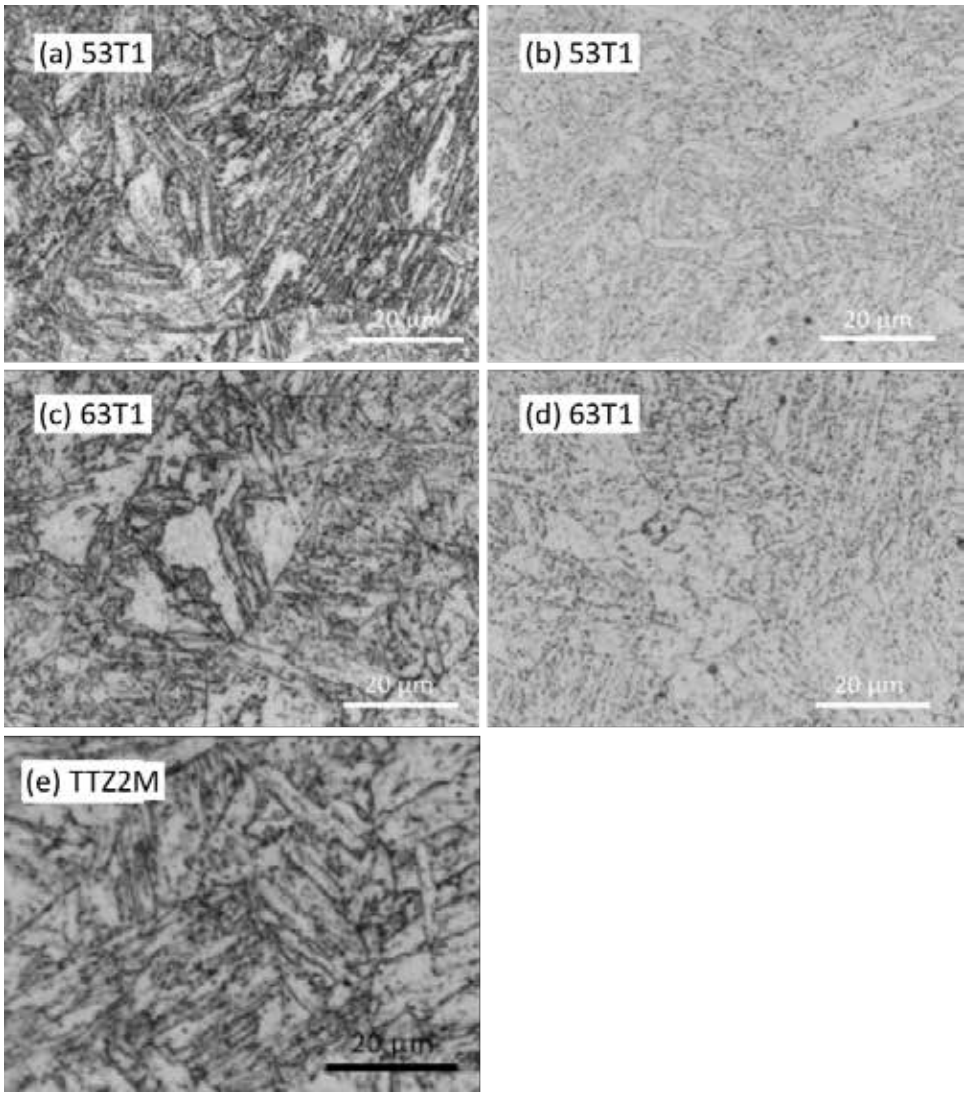

Figure 18. Optical micrographs of (a,b) 53T1 (91TT), (c,d) 63T1 (91TTa), and (e) TTZ2M subjected to two different etchants of (a,c,e) $50H_2O/5HNO_3/1HF$ solution and (b,d) 10 g oxalic acid in 100 ml distilled water.

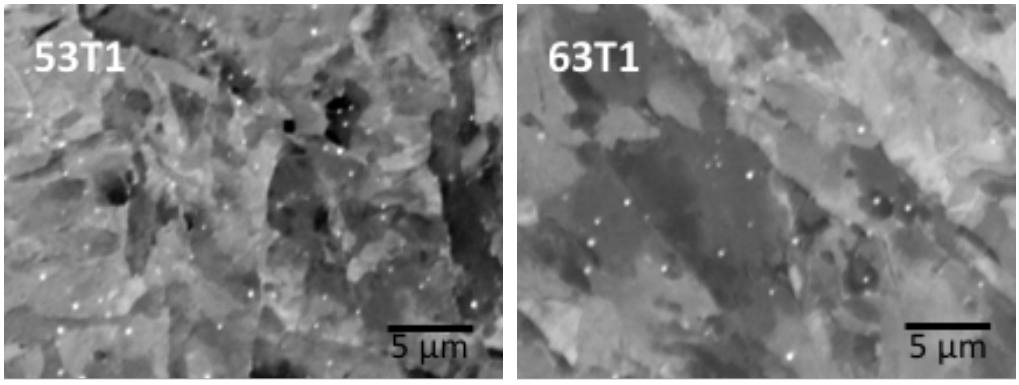

Figure 19. BSE images showing the ultrafine particles in the matrix of 53T1 (91TT) and 63T1 (91TTa).

4. BASIC MECHANICAL PROPERTIES

Vickers microhardness was evaluated using 1 kgf load with five measurements on the metallographically polished samples. Type SS-3 miniature specimens were extracted from the alloys with the length aligned with the rolling direction of the alloys for tensile tests. Figure 20 shows the specification of type SS-3 tensile specimen. Tensile tests were conducted in accordance with the American Society for Testing and Materials (ASTM) standard E8/E8M-13a, *Standard Test Methods for Tension Testing of Metallic Materials*, and E21/E21M-09, *Standard Test Methods for Elevated Temperature Tension Tests of Metallic Materials*. Tests were performed using an MTS tensile testing system with a load cell possessing 22 kN (5,000 lbf) capacity, which is integrated in the load train and placed in the water-cooled zone below the hot zone of the furnace. Due to the small specimen size, an extensometer was not used during the tests. Tensile testing was performed at a crosshead speed of 0.0076 mm/s (0.018 in./min), corresponding to a nominal strain rate of 0.001 s^{-1}. The tensile testing system, load cells, and furnace thermocouples were regularly calibrated.

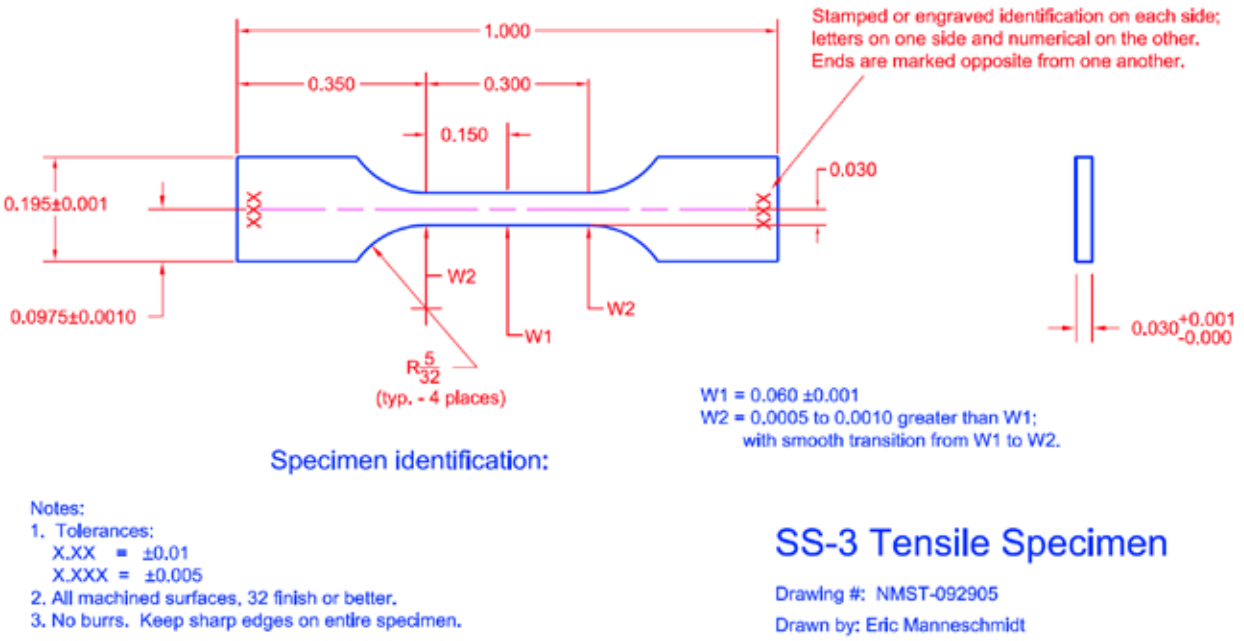

Figure 20. Specification of type SS-3 miniature tensile specimen (unit: inch).

Table 9 lists the average hardness and standard deviation of five measurements from each alloy sample. The hardness results of the Z3N4 and Z3N7 aged at 1000° for 336 h and 700°C for 1275 h are included. The aging treatments slightly reduced the hardness of the two ferritic alloys. The higher Ni content in Z3N7 seems to increase its hardness, compared to Z3N4. Ferritic alloys Z2N13 and 2573 showed a comparable low level of hardness, which are significantly lower than Z3N4 and Z3N7. In contrast, Z1N33A showed the highest hardness on the order of 320 HV1, which is likely attributable to the large amount of ultrafine particles of B2 phase as shown in Figure 13b, 15c-d, and 16c. The ferritic-martensitic steels 53T1 (91TT), 63T1 (91TTa), and TTZ2M showed hardness in the range of about 210 to 250 HV1, approximately similar to the Z3N4 and Z3N7 ferritic alloys.

Table 9. Vickers hardness (HV1) of the designed alloys listed in Table 1.

Alloy ID	As-fabricated	Annealed at 1000°C	Annealed at 700°C
Z3N4	220.8 ± 2.6	210.8 ± 4.4 (336 h)	208.6 ± 2.5 (1275 h)
Z3N7	252.6 ± 1.8	240.0 ± 4.8 (336 h)	249.3 ± 1.2 (1275 h)
Z2N13	156.6 ± 4.4		
Z1N33A	322.7 ± 5.5		
2573	151.7 ± 6.5		
53T1 (91TT)	211.2 ± 1.3		
63T1 (91TTa)	215.1 ± 1.8		
TTZ2M	251.4 ± 0.9		

A number of ferritic alloys with variant Ni and Zr content were developed, including those developed in a previous project. Figure 21a-b show the effects of Ni and Zr content on Vickers hardness of the Fe-12Cr-xNi-yZr ferritic alloys. Both Ni and Zr noticeably increase the hardness of the materials. Figure 21c plots the effect of Ni content on tensile tests results at room temperature of Fe-12Cr-6Zr-2W-xNi alloys. Consistent with the hardness results in Figure 21a, the yield and tensile strength increased with the increasing Ni content, with compromising uniform and total elongation. The strength increase with ductility reduction seems to be saturated when Ni content is above ~4 wt.%. A small amount of Ni of ~0.5 wt.% tended to slightly reduce strength with somewhat increase in ductility. The included results of Fe-12Cr-3Zr-2W-4Ni alloy showed lower strength with increased ductility, compared to the Fe-12Cr-6Zr-2W-4Ni alloy. The screening tests suggest that this type of ferritic alloys should have Ni < ~4 wt.% and Zr < ~3 wt.% for a better strength-ductility combination.

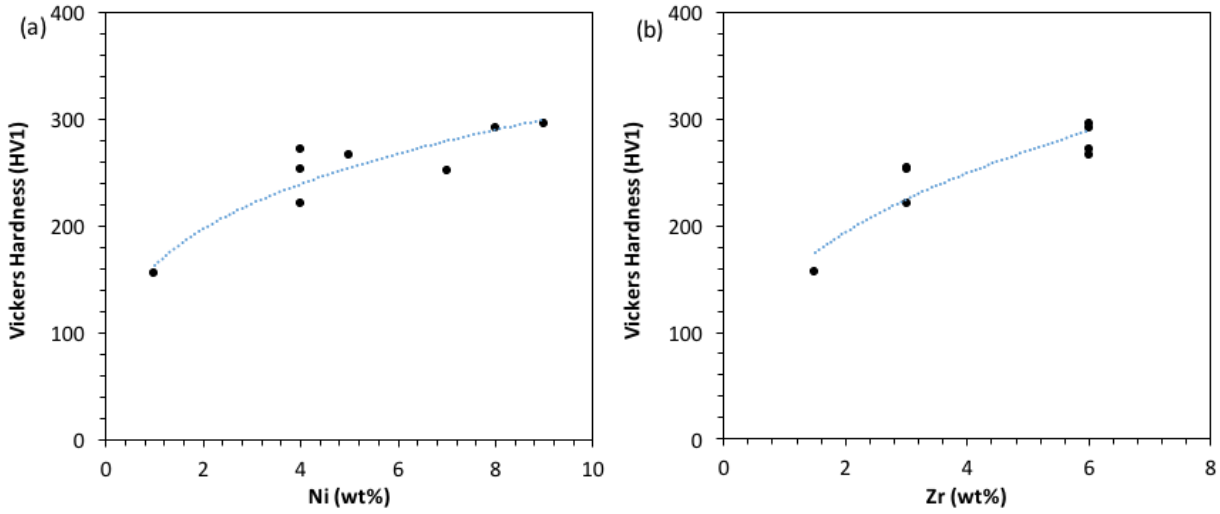

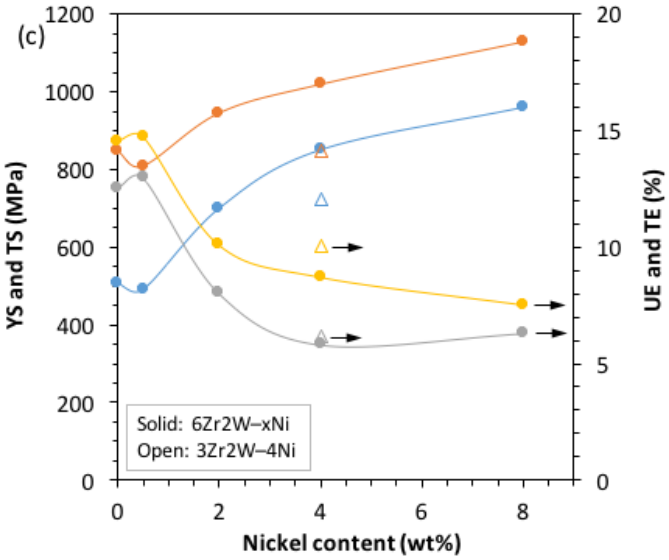

Figure 21. Effects of nickel and zirconium content on (a-b) Vickers hardness of Fe-12Cr-xNi-yZr alloys and (c) yield and tensile strength and uniform and total elongation of Fe-12Cr-6Zr-2W-xNi alloys, together with Fe-12Cr-3Zr-2W-4Ni alloy, at room temperature.

Tensile test results of 12Cr ferritic alloys Z2N13 and Z1N33A are plotted in Figure 22. Alloy Z2N13 showed lower strength with good ductility. In contrast, alloy Z1N33A had brittle fracture at room temperature despite excellent strength and acceptable ductility at temperatures above 400°C. The excellent strength is disminished at temperatures at and above 700°C. The brittle fracture at room temperature is likely caused by the pronounced coarse Laves particle strings at boundaries of the material as shown in Figure 15a. Alloy optimization has been initiated to eliminate the strings.

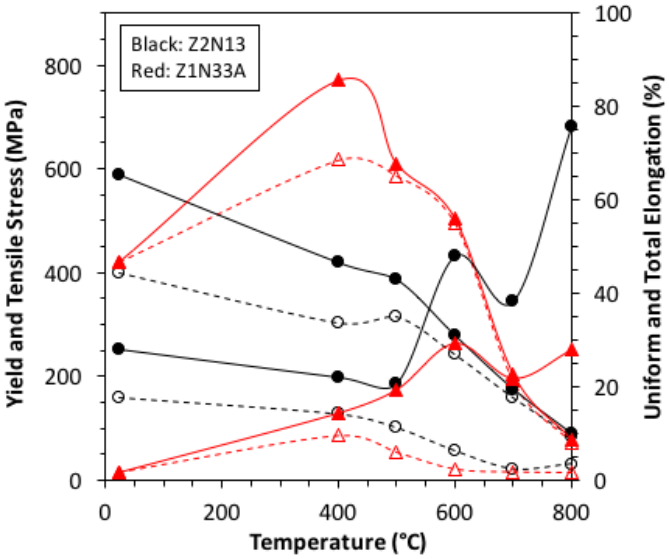

Figure 22. Temperature-dependent yield and tensile stress and uniform and total elongation of 12Cr ferritic alloys Z2N13 and Z1N33A. Open symbols with dashed lines denote the yield stress and uniform elongation; filled symbols with solid lines denote the tensile stress and total elongation.

Hardness and tensile tests were also conducted on the 9Cr alloys of 91TT (53T1) and 91TTa (63T1). The Vickers hardness of the control and thermomechanically treated (TMT) conditions of the alloys were plotted in Figure 23. Two types of TMT were recently applied to the two alloys by rolling at either 700°C (TMT1) or 600°C (TMT2) after normalization at 1130°C for 50 min, which was followed by tempering at 750°C for 1 h. The TMT1 led to significant increases in hardness by nearly 200% from the control (normalization + tempering) condition. In contrast, the TMT2 only led to a small increases in hardness. Microstructures of the two TMT conditions are initiated to elucidate the difference.

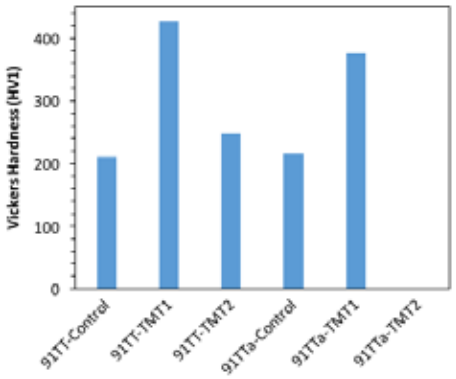

Figure 23. Vickers hardness of the two 9Cr alloys (91TT and 91TTa) in the control and TMT conditions.

The SS-3 samples of 91TT, 91TTa, and TTZ2M in the control (normalized + tempered) condition were tested at temperatures up to 800°C. The yield and ultimate tensile strength and uniform and total elongation of tested samples are plotted in Figure 24. The tensile results of strength and ductility, together with the Vickers hardness, do not show much difference between 91TT and 91TTa, given the different fractions of $M_{23}C_6$ and MX as expected in Figure 5. In contrast, TTZ2M showed noticeably higher strength with slightly compromised ductility. The strength of 91TT and 91TTa are greater than the tensile strength of Z2N13 at temperatures up to 600°C, which becomes comparable to Z2N13 and Z1N33A at 700 and 800°C.

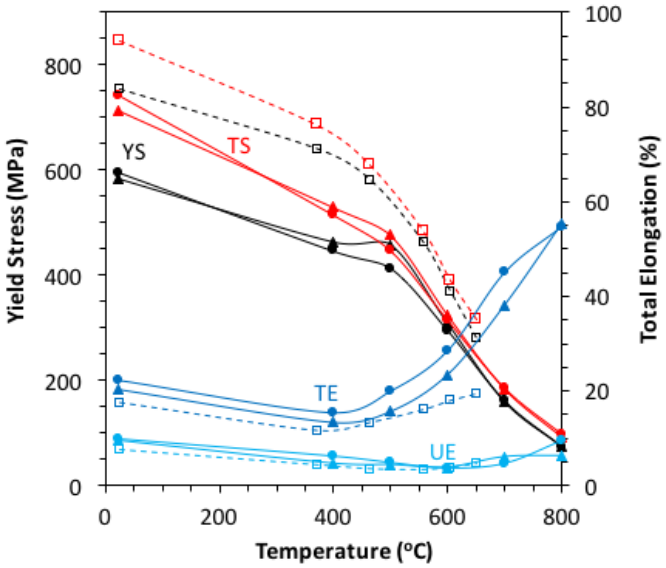

Figure 24. Temperature-dependent yield and tensile strength and uniform and total elongation of the 9Cr ferritic-martensitic steels 53T1 (91TT), 63T1 (91TTa), and TTZ2M in circles, triangles, and squares, respectively.

5. ION IRRADIATION EXPERIMENTS AND PRELIMINARY RESULTS

Ion irradiation and post-irradiation examination were conducted at the University of Wisconsin-Madison with a NEC 1.7MV Tandem accelerator, for the alloys listed in Table 10. A 5 mm by 4 mm sample of each alloy was ground from 800 grit to 1200 grit and thoroughly polished through a sequence of five steps, starting from MD Mol (Diamat Rigid Magnetic Disc) with 3 μm Diamond Paste to MD Chem (Chem-Pol Rigid Magnetic Disc) with 0.02 μm colloidal silica. The grinding and polishing procedure for sample preparation took 8-9 hours. The cleaning procedure involved sonicating the samples for 10 minutes in acetone bath, deionized water bath, and followed finally with cleaning in an ethanol bath. Zygo New View, a white light interferometer, was used to take five different surface profiles across different regions of the samples for each alloy. The roughness measurements were taken with cylinder correction to account for the possible uneven surface of the samples, potentially caused during sample preparation. Figure 25 presents the example of surface profiles from alloys Z3N4, Z3N7, 53T1, and 63T1, under cylinder correction, which yielded surface roughness of 37.4, 18.2, 31.8, and 34 nm, respectively.

Table 10. Alloy samples in a size of 4 mm×5 mm×1 mm, used in the two batch of irradiation.

Irradiation batch	Irradiation condition	Sample	Quantity (pieces) received by UW from ORNL
Run 1	349±12°C, $(6.2\pm1.2)\times10^{12}$ ion/cm^2/s	91TT	10
		91TTa	10
		TTZ2M	12
		Z3N7	12
		Z1N33A	12
		Z2N13	12
Run 2	343±21°C, $(5.9\pm1.3)\times10^{12}$ ion/cm^2/s	Z3N4	12
		2573	12

The irradiating ion is Fe^{2+} with a energy of 4.0 MeV. The nominal damage level received by each sample is 100 dpa on average, with the peak damage being 218 dpa at the depth of 1.10 μm. The damage profile is shown in Figure 26, with superimposed ion concentration profile. Both profiles were simulated using the Kinchin-Pease Model in the Stopping and Range of Ions in Matter (SRIM) software, with the irradiated material being in 87Fe-11Cr-2Ni (average composition of all the alloys in Table 10) and the displacement energies of Fe, Cr and Ni being 40 eV. During irradiation, the vacuum of the chamber is in the range of 2×10^{-6} - 5×10^{-7} Torr. The irradiation temperature was monitered by two thermocouples attached to the opposite corners of the sample stage. The flux was calculated from ion beam current and beam scanning area of 2 cm^2. The temperature and flux profiles were plotted in Figure 27a and b, for Run 1 and 2 in Table 10, respectively. Occasional positive or negative flux spikes resulted from spikes of ion current or possibly secondary electron currents. In run 1, temperature is 349 ± 12 °C and flux is $(6.2 \pm 1.2) \times 10^{12}$ ion/cm^2/s. In run 2, temperature is 343 ± 21 °C and flux is $(5.9 \pm 1.3) \times 10^{12}$ ion/cm^2/s.

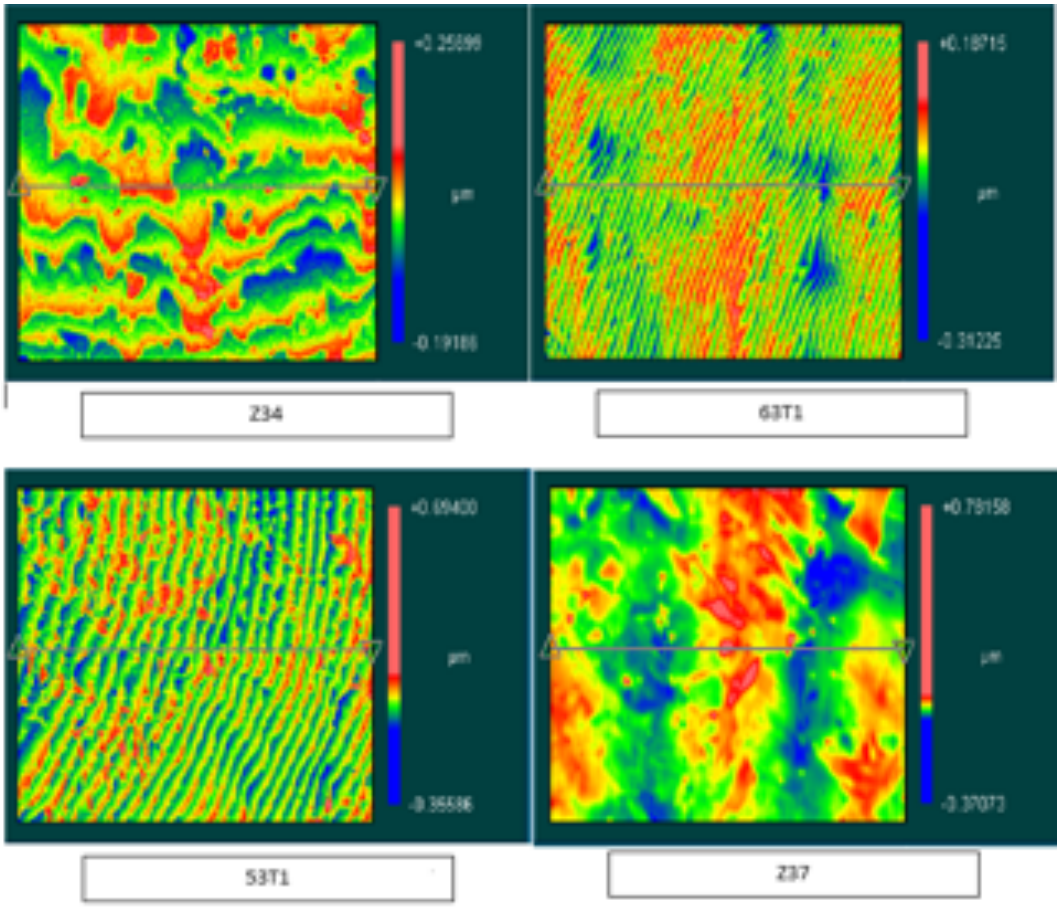

Figure 25. Surface profiles obtained form the Zygo New View (white light interferometer) of alloys Z3N4, Z3N7, 53T1, and 63T1.

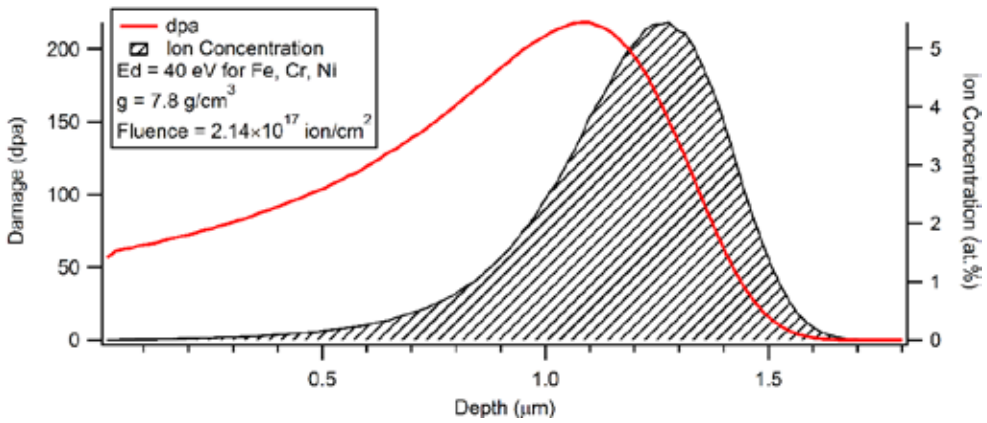

Figure 26. 4 MeV iron induced damage in 87Fe-11Cr-2Ni, the average composition of eight alloys in Table 1. The damage and implantation profiles were calculated using the Kinchin-Pease Model in the Stopping and Range of Ions in Matter (SRIM) software. *Ed* is atom displacement energy.

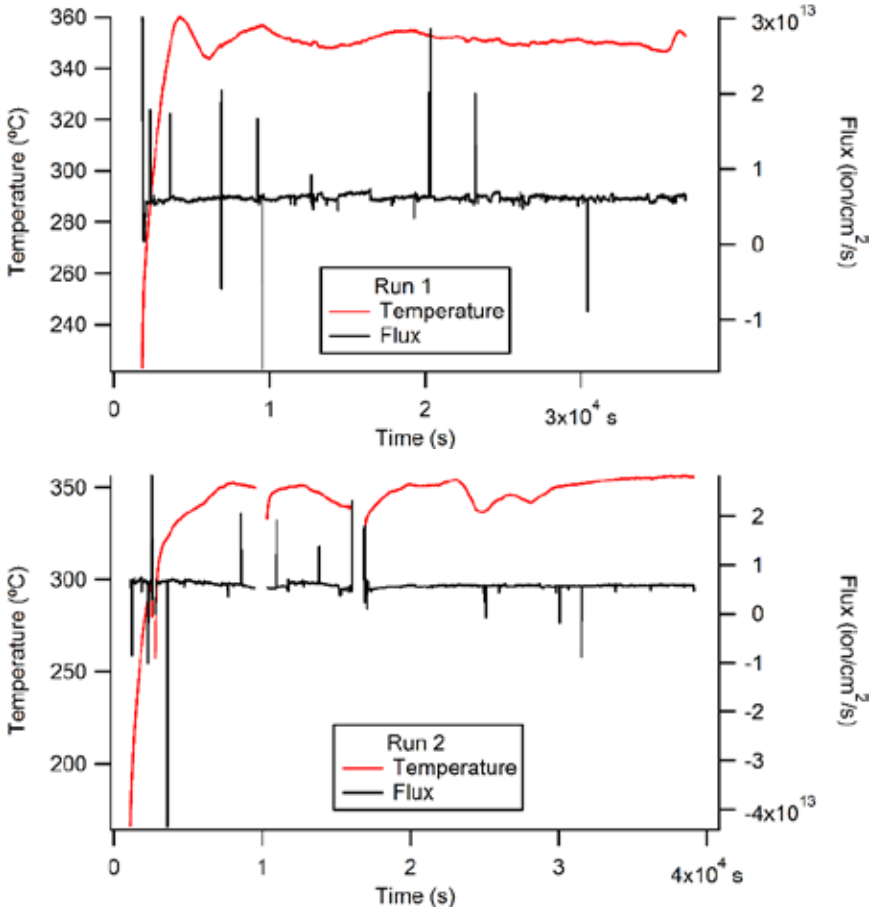

Figure 27. Temperature and flux during 4 MeV iron irradiation. (a) Irradiation run 1 consisting of 91TT, 91TTa, TTZ2M, Z3N7, Z1N33A, Z2N13. (b) Irradiation run 2 consisting of Z3N4, 2573.

Figure 28 shows the sample picture after irradiation. Samples are labeled as "alloy label - 1". A small part of the samples was masked from irradiation. The irradiated parts are darker but still reflective, which provides a qualitative indication that any oxide layer formed during irradiation is very thin. The height difference across the mask boundary as measured by high accuracy profilometry will allow us to analyze swelling, if any.

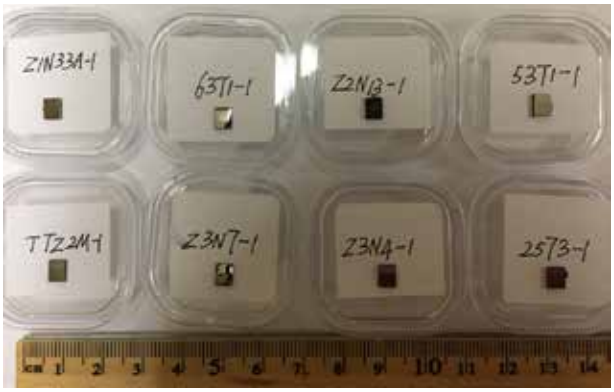

Figure 28. The samples received 100 dpa Fe^{2+} irradiation at 350 °C

Minimal radiation-induced hardness change is desirable for nuclear structural materials. Figure 29 shows hardness of alloys Z2N13 and Z3N7 measured by nanoindentation. A Hysitron TI-950 TriboIndenter with a Berkovich tip and a High Load transducer was used with indentation depths of 1 μm, 2 μm, 4 μm, 6 μm, and 8 μm. Both the unirradiated part (the brighter part shown in Figure 28) and irradiated part were measured, since these two regions have experienced the same thermal history.

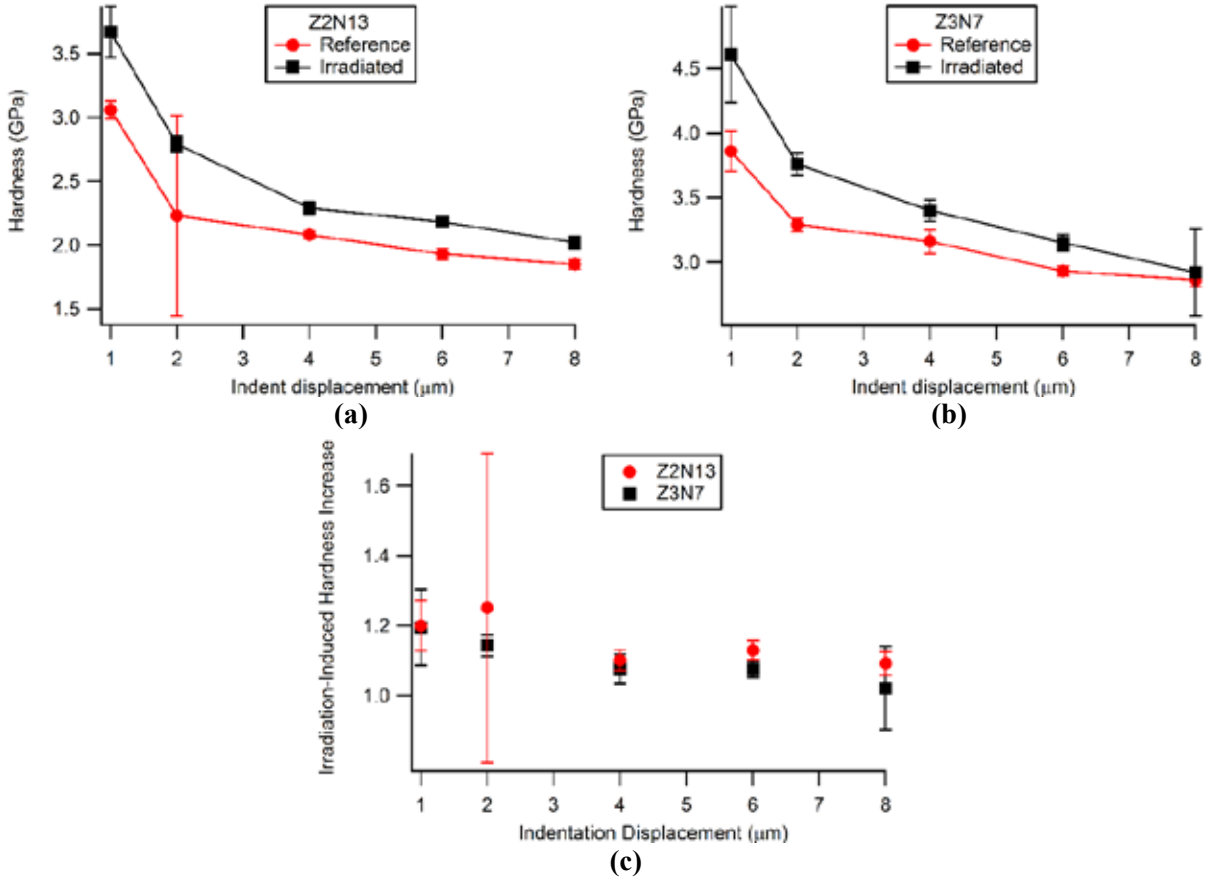

Figure 29. Hardness and irradiation induced hardness increase in Z2N13 and Z3N7. (a) Hardness of the same Z2N13 sample from masked unirradiated region (reference) and irradiated region. (b) Hardness of Z3N7. (c) Hardness ratio of irradiated / reference.

SEM characterization of ion irradiated specimens has been conducted using a JEOL JSM-6610. Figure 30 shows secondary electron images of Zr-containing alloys Z1N33A (a), Z2N13 (b-c), Z3N4 (d-e), and Z3N7 (f-g). Both unirradiated (Figure 30a left, Figure 30b, d, f) and irradiated (Figure 30a right, Figure 30c, e, g) regions exhibit network-like secondary phase. X-ray energy dispersive spectroscopy (EDS) shows that the secondary phase is rich in Zr.

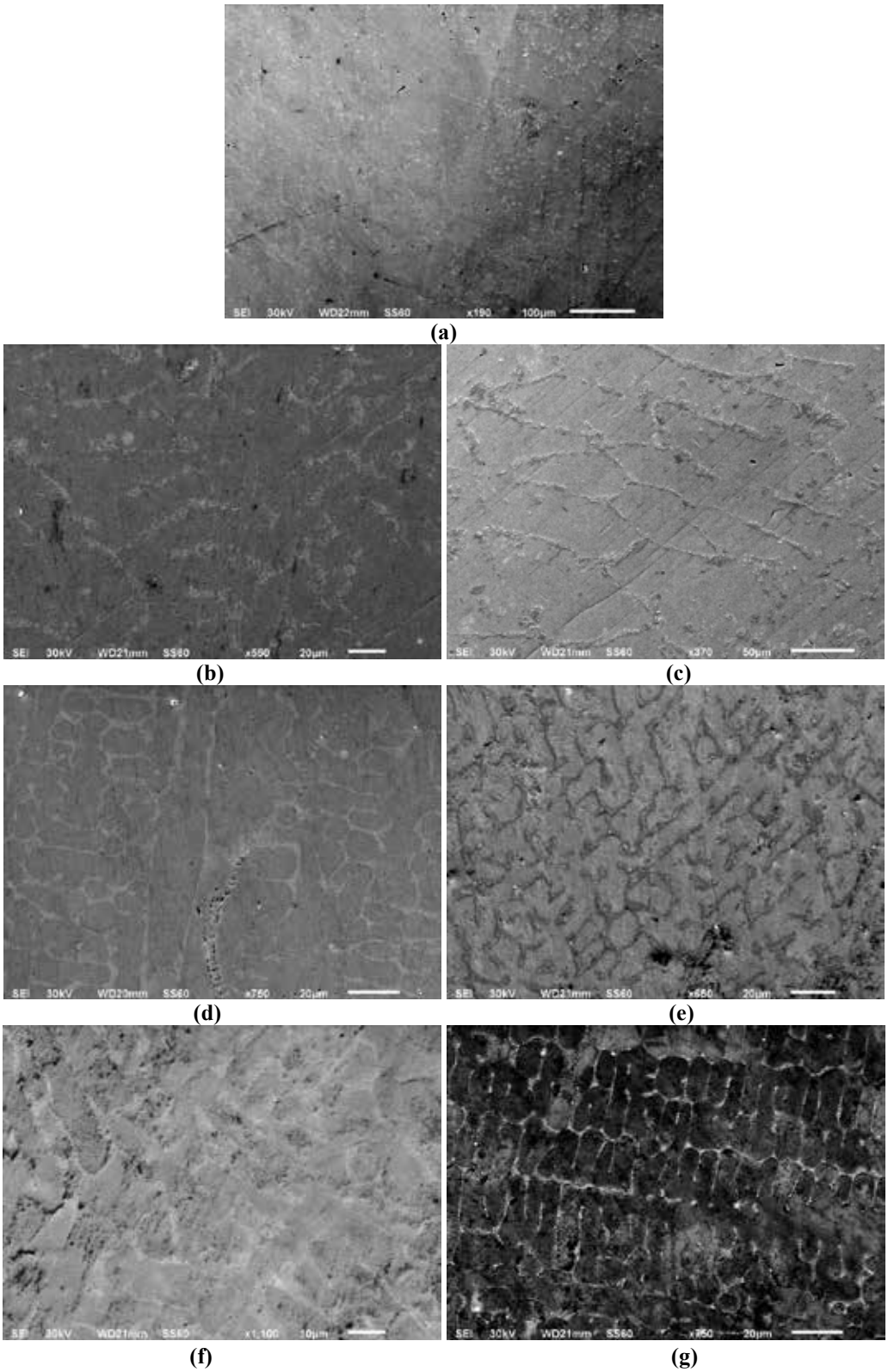

Figure 30. Secondary electron images of Zr-containing ferritic alloys. (a) Z1N33A. Irradiation boundary is visible as the straight line across the central part of image from top right to bottom center. Left is unirradiated. Right is irradiated. (b) Unirradiated Z2N13. (c) Irradiated Z2N13. (d) Unirradiated Z3N4. (e) Irradiated Z3N4. (f) Unirradiated Z3N7. (g) Irradiated Z3N7.

Figure 31 shows secondary electron images of 91TT (53T1) and 91TTa (63T1) near irradiation boundary. In Figure 31a, the irradiated 91TT is at left of the boundary. In Figure 31b, the irradiated 91TTa is on the right. There are Ti-rich particles and Ta rich particles in 91TT. Figure 31b-d presents images and EDS of 91TTa. EDS in Figure 31d was acquired from the hexagonal feature in Figure 31c and nearby matrix. EDS of the hexagonal feature shows much lower Fe Lα peak (0.70 keV) than the matrix does, indicating that it is a sidewall of a hole that absorbs low energy x-rays. The faceted holes are present in both unirradiated and irradiated 63T1, as shown in Figure 31b. Secondary phase particles in 91TTa include Ta and Ti-rich precipitates and Ti-rich precipitates.

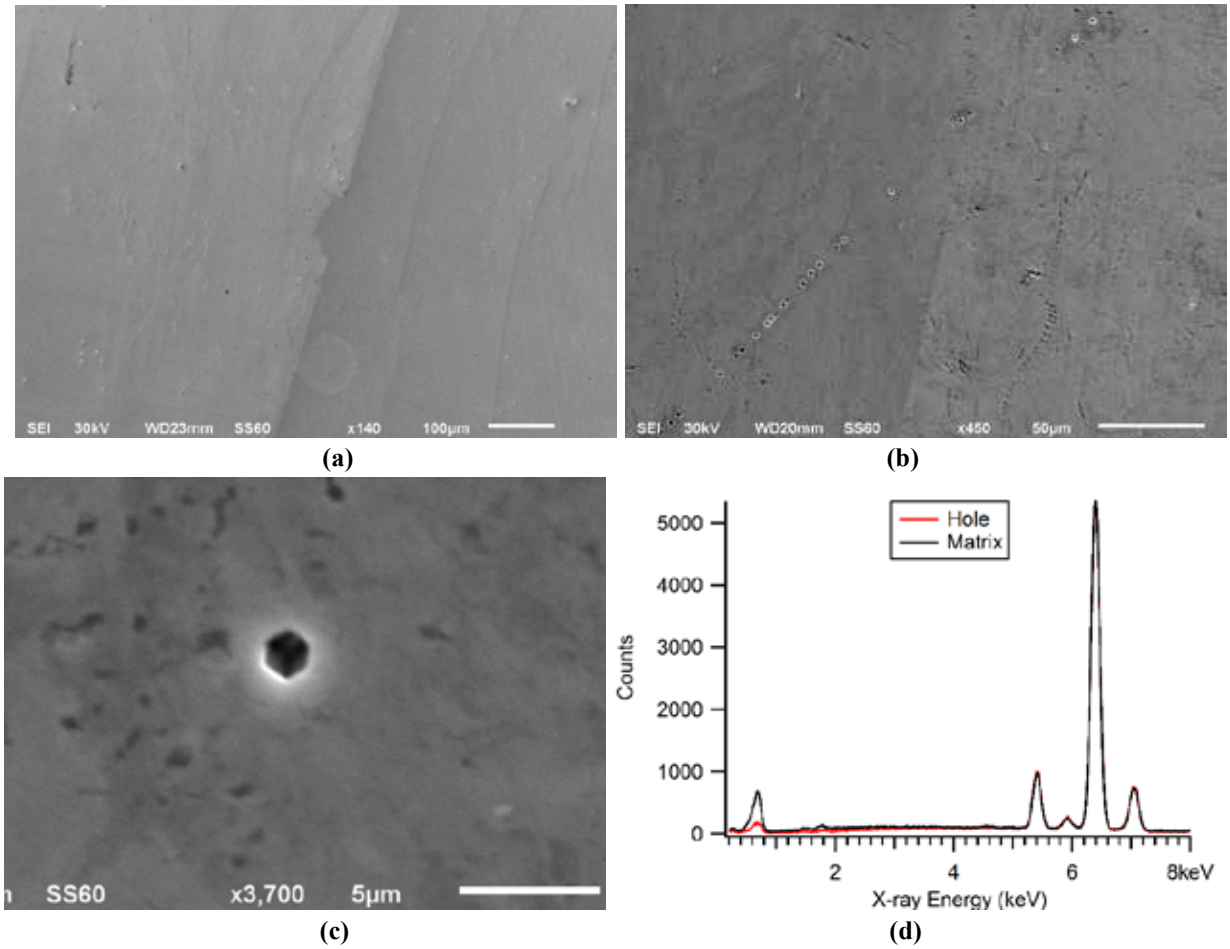

Figure 31. Secondary electron images of alloys 91TT and 91TTa. (a) 91TT: left side of the image is irradiated and right side is unirradiated. (b) 91TTa: left side of image is unirradiated and right is irradiated. (c) Irradiated 91TTa. (d) EDS collected at the hole in (c) and nearby matrix.

Figure 32 shows secondary electron image of alloy 2573 near irradiation boundary. Left side of the sample is unirradiated and right is irradiated. Fine granular contrast < 0.5 µm is present in the irradiated matrix of the alloy. There are dark gray particles several microns long in irradiated 2573 in Figure 32 (right side). EDS analysis indicated these particles to be rich in both Nb and Ti. The white particles in Figure 32 (left side) are CaO contaminant.

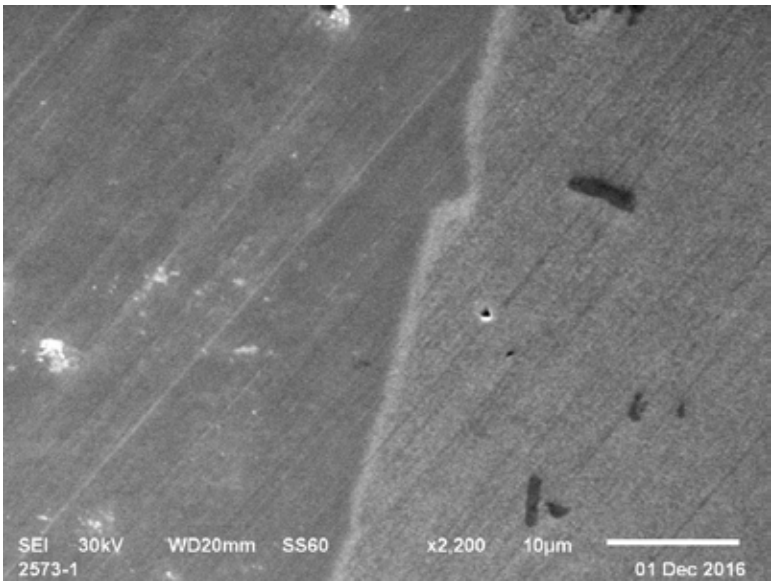

Figure 32. Secondary electron image of 2573. Left part is unirradiated. Right part is irradiated.

Figure 33 displays the secondary electron images of TTZ2M. There are square shaped particles in both unirradiated (Figure 33a) and irradiated (Figure 33b) regions. They are rich in Nb and Ti. The particles are likely to be (Nb,Ti)N according to the size and morphology of the particles. Some "cracks" are present in irradiated TTZ2M, as shown by the bright curvy lines in Figure 33b, which were likely resulted from the hot-rolling processing because the samples were extracted from the the locations close to the side/edge of the rolled alloys.

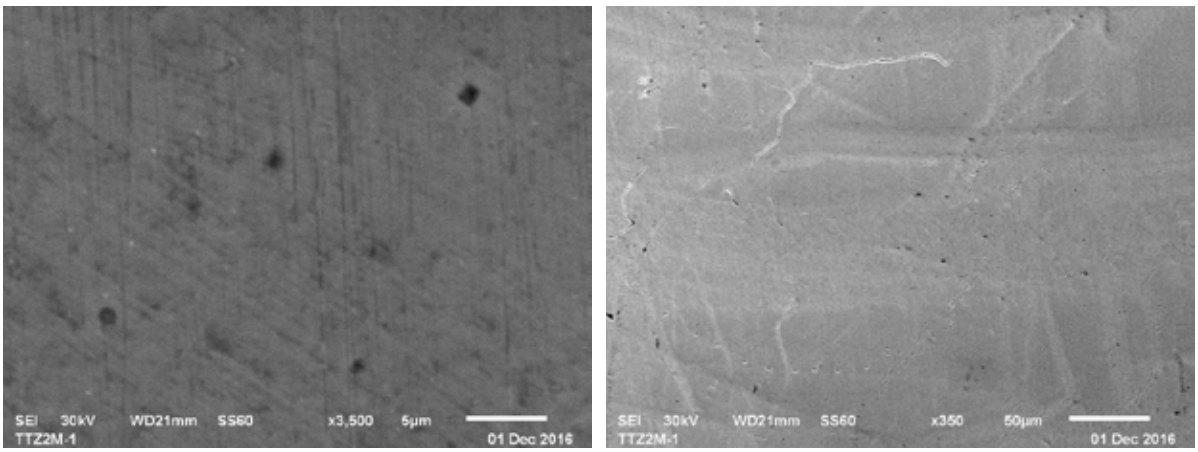

(a) **(b)**

Figure 33. Secondary electron images of TTZ2M. (a) Unirradiated TTZ2M. (b) Irradiated TTZ2M.

Table 11 summarizes SEM evaluation of the microstructure at surface of the alloys. Particle size appears to increase slightly after irradiation in 91TTa and TTZ2M. Zr-containing alloys all have network like Zr-rich phase, primarily Laves phase. The Zr-rich secondary phase volume increases with Zr concentration. As the secondary phase impedes dislocation movement, Z3N7 is harder than Z2N13, as verified by nanoindentation measurements (Figure 29).

Table 11. SEM measured surface microstructure of alloys.

Sample	Secondary phase /surface features	Particle size (μm)	Particle area density (m^{-2})
91TT	Ti-rich, Ta-rich particles	0.5 ± 0.1 (Irradiated)	6.5×10^{9} (Irradiated)
91TTa	Faceted holes, TaTi-rich particles	0.7 ± 0.5 (Reference) 0.8 ± 0.3 (Irradiated)	3.1×10^{9} (Reference) 1.5×10^{9} (Irradiated)
TTZ2M	Cracks, NbTi-rich particles	0.7 ± 0.3 (Reference) 0.8 ± 0.2 (Irradiated)	2.3×10^{9} (Reference) 2.6×10^{9} (Irradiated)
2573	Fine granular contrast, NbTi-rich particles	1.2 ± 0.7 (Irradiated)	2.2×10^{9} (Irradiated)
Sample	Secondary phase/surface features	Zr-rich phase area / total surface area (%)	
Z1N33A	Network of Zr-rich phase	1.3 ± 0.5 (Irradiated)	
Z2N13	Network of Zr-rich phase	2.2 ± 0.5 (Irradiated)	
Z3N4	Network of Zr-rich phase	13 ± 3 (Irradiated)	
Z3N7	Network of Zr-rich phase	6 ± 4 (Irradiated)	

6. CONCLUSIONS AND FUTURE WORK

With the aid of computational thermodynamics, Ni was identified to suppress the liquidus temperature of Fe_2Zr. Four Fe-Cr-Ni-Zr alloys, i.e., Z3N4, Z3N7, Z6N5, and Z6N9, were designed to study the Ni effect on the phase stability of Fe_2Zr Laves_phase. These alloys were fabricated through traditional arc-metling, followed by annealing at 1000°C for 336 hours and 700°C for 1275 hours. The microstructure were examined and characterized by SEM imaging, EDS, XRD, and TEM analyses. It was found that the phases in equilibrium with the matrix bcc phase are C15_Laves phase and $Fe_{23}Zr_6$ phase. The volume fraction of the intermetallic phases increased with the increasing Ni and Zr content. Instead of $(Fe,Cr)_2Zr$ C14_Laves phase, Ni stabilizes the C15_Laves structure in the Fe-Cr-Ni-Zr alloys by substituting Fe and Cr atoms with Ni atoms in the first sublattice. Addition of Ni also stabilized $Fe_{23}Zr_6$, which is metastable in the Fe-Cr-Zr ternary system. Additionally, Ni_7Zr_2 phase was observed in samples with high Ni/Zr ratio. Increasing the Zr and Ni content noticeably increased the hardness and strength of the alloys because of the increased fraction of intermetallic phases. The results suggest that this type of ferritic alloys should have Ni < ~4 wt.% and Zr < ~3 wt.% for balanced strength and ductility. The microstructural and composition results obtained from this study was incorportated into the the Fe-Cr-Ni-Zr database for further alloy design.

Two 12Cr ferritic alloys, i.e., Z2N13 and Z1N33A, were designed and fabricated to investigate effect of Laves phase and B2-NiAl phase on mechanical properties and radiation resistance. Compared to the 10–20 μm grain size of Z2N13, the grain size of Z1N33A is about one order of magnitude larger. The high density (10^{22} m^{-3}) of ultrafine (~11 nm) B2-NiAl precipitates in Z1N33A significantly increased the strength of the alloy at temperatures below 700°C. However, coarse Laves particle strings decorating boundaries resulted in brittle fracture of the alloy at room temperature. Alloy optimization will be proposed to eliminate the coarse Laves phase strings for satisfactory strength-ductility combination. Two 9Cr ferritic-martensitic steels, i.e., 91TT (53T1) and 91TTa (63T1), were designed to have different amounts of $M_{23}C_6$ and MX precipitates to understand the effects of the two types of precipitates on strength and radiation resistance. However, the two steels in the normalized and tempered condition did not exhibit significant differences in microstructures and tensile properties. Further microstructural characterization is in progress to elucidate this observation. Two TMTs were applied to the two steels, leading to significant or moderate increases in Vickers hardness. Microstructural characterization and tensile tests are in progress to understand the TMT effects.

One set of samples from eight of the ferritic and ferritic-martensitic alloys, i.e., Z3N4, Z3N7, Z2N13, Z1N33A, 2573, 53T1, and 63T1, was irradiated in two runs at 349 ± 12°C and 343 ± 21°C with 4 MeV Fe^{2+} for up to 2.14×10^{17} ion/cm^2. The irradiation is expected to have a peak damage of ~218 dpa at 1.1 μm under surface according to the SRIM simulation. Post-irradiation characterization is in progress. Preliminary results indicated that all the irradiated samples had smooth and reflective surface. Similar radiation-induced hardening by ~20% at 1 μm indentation depth was observed on both Z2N13 and Z3N7. Irradiation resulted in a slight increase in precipitate size in 63T1 and TTZ2M. Detailed characterization is in progress.

Plans for Next Year

- Optimize a few ferritic alloys, favoring fine Laves phase and ultrafine B2-NiAl phase, to achieve balanced strength and ductility.
- Characterize radiation-induced amorphorization of intermetallic phases, e.g., $Fe_{23}Zr_6$ and Cr15-Laves, and its effect on nanoindentation behavior.
- Complete nanoindentation measurement of the irradiated samples in the two runs.
- Characterize microstructural evolution of the irradiated samples in the two runs.
- Conduct new irradiation experiments using 4 MeV Fe^{2+} for up to 220 dpa (peak dose) at 475°C and 600 °C on selected alloy samples.

REFERENCES

[1] Zinkle SJ, Snead LL. Annual Review of Materials Research 2014;44:241.
[2] Raj B, Vijayalakshmi M. RJM Konings, TR Allen, RE Stoller, S. Yamanaka, Comprehensive Nuclear Materials, Elsevier 2012.
[3] Tan L, Yang Y. Metallurgical and Materials Transactions A 2015;46:1188.
[4] Hellstern E, Schultz L. Materials Science and Engineering 1988;97:39.
[5] Castaño F, Stobiecki T, Gibbs M, Czapkiewicz M, Kopcewicz M, Gacem V, Speakman J, Cowlam N, Blythe H. Journal of Physics: Condensed Matter 1997;9:10603.
[6] Byeli A, Kukareko V, Kononov A, Bilenko E. Journal of Surface Investigation. X-ray, Synchrotron and Neutron Techniques 2008;2:340.
[7] Yu K, Fan Z, Chen Y, Song M, Liu Y, Wang H, Kirk M, Li M, Zhang X. Materials Research Letters 2015;3:35.
[8] Tan L. Development and Mechanical Results of Zr-Bearing Ferritic Steels. Oak Ridge National Laboratory (ORNL), ORNL/TM-2015/595, 2015.
[9] Lu Z, Liu C. Acta Materialia 2002;50:3501.
[10] Takeuchi A, Inoue A. Materials Transactions 2005;46:2817.
[11] Johnson WL. Fundamental aspects of bulk metallic glass formation in multicomponent alloys. Materials science forum, vol. 225: Trans Tech Publ, 1996. p.35.
[12] Ma D, Cao H, Ding L, Chang YA, Hsieh K, Pan Y. Applied Physics Letters 2005;87:171914.
[13] Yan X-Y, Chang Y, Yang Y, Xie F-Y, Chen S-L, Zhang F, Daniel S, He M-H. Intermetallics 2001;9:535.
[14] Kaufman L, Bernstein H. 1970.
[15] Yang Y, Chen T, Tan L. Computational thermodynamic aided design of novel ferritic alloys. ORNL/TM-2016/229, June 30, 2016.
[16] Yang S, Zhang J, Wang C, Yu W, Shi Z, Liu X. Experimental investigation of phase equilibria in the Ni–Fe–Zr ternary system. J. Mater. Res. 2016;31(16):2407–2414.
[17] Abraham D, Richardson Jr. J, McDeavitt S. Formation of the Fe23Zr6 phase in Fe-Zr alloy. Scripta Mater. 1997;37(2):239–244.
[18] Abraham D, Dietz N. Role of Laves intermetallics in nuclear waste disposal. Mater. Sci. Eng., A 2002;329-331:610–615.
[19] Ohodnicki Jr P, Cates N, Laughlin D, McHenry M, Widom M. Physical Review B 2008;78:144414.
[20] Stein F, Sauthoff G, Palm M. Journal of Phase Equilibria 2002;23:480.
[21] Yang Y, Tan L, Bei H, Busby JT. Journal of Nuclear Materials 2013;441:190.
[22] Muraoka Y, Shiga M, Nakamura Y. physica status solidi (a) 1977;42:369.